Towards integrated photonic interposers for processing octave-spanning microresonator frequency combs

Ashutosh Rao,[1,2,*] Gregory Moille,[1,3] Xiyuan Lu,[1,2] Daron A. Westly,[1] Davide Sacchetto,[4] Michael Geiselmann,[4] Michael Zervas,[4] Scott B. Papp,[5,6] John Bowers,[7] and Kartik Srinivasan[1,3,†]

[1]*Microsystems and Nanotechnology Division, Physical Measurement Laboratory, National Institute of Standards and Technology, Gaithersburg, MD 20899, USA*

[2]*Maryland NanoCenter, University of Maryland, College Park, MD 20742, USA*

[3]*Joint Quantum Institute, NIST/University of Maryland, College Park, MD 20742, USA*

[4]*Ligentec, EPFL Innovation Park, Batiment C, Lausanne, Switzerland*

[5]*Time and Frequency Division, Physical Measurement Laboratory, National Institute of Standards and Technology, Boulder, CO 80305, USA*

[6]*Department of Physics, University of Colorado, Boulder, CO 80309, USA*

[7]*Department of Electrical and Computer Engineering, University of California, Santa Barbara, CA 93106, USA*

*Email: ashutosh.rao@nist.gov

†Email: kartik.srinivasan@nist.gov

Author to whom correspondence should be addressed:

*K.S. (email: kartik.srinivasan@nist.gov; Microsystems and Nanotechnology Division, Physical Measurement Laboratory, National Institute of Standards and Technology, Gaithersburg, MD 20899, USA; Tel: +1 (301) 975-5938).

Email addresses for all contributing authors: Ashutosh Rao: ashutosh.rao@nist.gov, Gregory Moille: gregory.moille@nist.gov, Xiyuan Lu: xiyuan.lu@nist.gov, Daron A. Westly: daron.westly@nist.gov, Davide Sacchetto: davide.sacchetto@ligentec.com, Michael Geiselmann: mwg@ligentec.com, Michael Zervas: michael.zervas@ligentec.com, Scott B. Papp: scott.papp@nist.gov, John Bowers: bowers@ece.ucsb.edu, and Kartik Srinivasan: kartik.srinivasan@nist.gov.

ABSTRACT

Microcombs - optical frequency combs generated in microresonators - have advanced tremendously in the last decade, and are advantageous for applications in frequency metrology, navigation, spectroscopy, telecommunications, and microwave photonics. Crucially, microcombs promise fully integrated miniaturized optical systems with unprecedented reductions in cost, size, weight, and power. However, the use of bulk free-space and fiber-optic components to process microcombs has restricted form-factors to the table-top. Taking microcomb-based optical frequency synthesis around 1550 nm as our target application, here, we address this challenge by proposing an integrated photonics interposer architecture to replace discrete components by collecting, routing, and interfacing octave-wide microcomb-based optical signals between photonic chiplets and heterogeneously integrated devices. Experimentally, we confirm the requisite performance of the individual passive elements of the proposed interposer – octave-wide dichroics, multimode interferometers, and tunable ring filters, and implement the octave spanning spectral filtering of a microcomb, central to the interposer, using silicon nitride photonics. Moreover, we show that the thick silicon nitride needed for bright dissipative Kerr soliton generation can be integrated with the comparatively thin silicon nitride interposer layer through octave-bandwidth adiabatic evanescent coupling, indicating a path towards future system-level consolidation. Finally, we numerically confirm the feasibility of operating the proposed interposer-synthesizer as a fully assembled system. Our interposer architecture addresses the immediate need for on-chip microcomb processing to successfully miniaturize microcomb systems and can be readily adapted to other metrology-grade applications based on optical atomic clocks and high-precision navigation and spectroscopy.

INTRODUCTION

Optical microcombs, generated in micro and nanophotonic resonators, have substantially broadened the reach of applications of optical frequency combs[1]. Along with the promise of a dramatic transformation from traditional table-top and rack-mount form factors to chip-scale integrated systems, a variety of applications have been shown to benefit from the use of microcombs[2-4]. Furthermore, persistent innovation enabled by the precision nanofabrication of nanophotonic resonators continues to yield desirable and exotic optical microcombs[5-9] for next-generation systems. The convergence of nanophotonic resonators with scalable integrated photonics inherently supports the promise of creating integrated microcomb-based systems, with immediate applications in optical frequency synthesis[10-12], optical atomic clocks[13,14], optical distance ranging[15-17], optical spectroscopy[18-20], microwave and radiofrequency photonics[21-23], astronomy[24,25], and telecommunications[26-28].

However, to realize these integrated microcomb-based systems, integrated photonic interposers that connect and operate on optical signals that transit between the many constituent photonic components will be critical. In fact, the pursuit of such integrated systems has driven recent progress in active photonics, e.g., lasers[29–32] and detectors[33], nonlinear photonics in microresonators[5-9,34,35] and waveguides[36–39], and passive photonics and heterogeneous integration[40–42], and has motivated milestones such as the generation of microcombs using chip-scale lasers[43–45]. Photonic interposers that collect, filter, route, and interface light between many such active and passive devices are essential to realize the improvements in cost, size, weight, and power, performance, and scalability, offered by microcombs and integrated photonics, and will promote further system-level innovation using frequency combs. Such interposers need to integrate multiple broadband high-performance photonic elements, manage octave-wide light, and maintain modal and polarization purity in a low loss and high damage threshold photonics platform while pragmatically balancing heterogeneous integration and chip-to-chip coupling on a system-level architecture.

In this work, we consider integrated photonic interposers in the context of optical frequency synthesis. Optical frequency synthesis is one application in which the transition from lab-scale instrumentation to deployable technology hinges on the ability to combine microcomb technology with other integrated photonics. Optical frequency synthesizers generate stable, accurate, and precise optical frequencies from a standard microwave reference, have traditionally used mode-locked solid-state and fiber lasers to derive a fully stabilized self-referenced frequency comb[10,11], and are indispensable in frequency metrology and timekeeping[13,46], coherent light detection and ranging[15], spectroscopy[18], microwave synthesis[21], and astronomy[24]. Yet, the cost and size of such table-top systems has limited their widespread application.

While substantial progress has been made recently towards optical frequency synthesis using integrated photonic devices[12,47-51], these nascent efforts have required the use of free-space and fiber-optic components that hinders the overall goal of having standalone chip-size microcomb systems. These efforts have employed microcombs in on-chip silicon nitride and silica microresonators[12,47] and bulk crystalline resonators[48], supercontinuum and second harmonic generation in nonlinear silicon-on-insulator waveguides[51], and phase-locking in indium phosphide photonic integrated circuits[48,49]. Each of these photonic platforms offers different devices and functionality that are beneficial to building an integrated optical frequency synthesizer.

Here, we propose an integrated photonics interposer architecture for a microcomb-based optical frequency synthesizer that collects, routes, and interfaces broadband light from discrete chiplets and heterogeneously integrated photonic devices. We experimentally demonstrate the constituent passive elements of the proposed interposer, i.e., octave-wide dichroic couplers, resonant filters, and multimode interferometers, and confirm that their performance agrees with our electromagnetic simulations via short-loop tests. The remaining heterogeneous integration-based components have been reported elsewhere previously[33,39,42]. We use the silicon nitride (Si_3N_4) photonic platform, based on requirements of low absorption, high damage threshold, and broad optical transparency. We directly verify the suitability of the dichroics to process octave-wide light by using an octave-spanning microcomb generated in a thick silicon nitride chip as the input. Subsequently, we demonstrate the octave-wide spectral processing of an octave-spanning microcomb, key to the interposer, via an integrated sequence of the dichroic couplers and a tunable ring filter, measuring spectral contrast between the optical bands of interest that is appropriate for our intended application and congruent with our short-loop characterization of the individual components. Further, we report the single-chip integration of a broadband

Si_3N_4 microcomb generated in a thick Si_3N_4 layer with the thinner Si_3N_4 photonic layer used for the interposer components, demonstrating a route towards additional system-level consolidation. Finally, we numerically confirm the feasibility of our proposed scheme for an integrated photonics interposer for frequency synthesis through a detailed system-level analysis, calculating the signal-to-noise ratios for the expected constituent beat notes based on the experimentally-demonstrated performance of the different components.

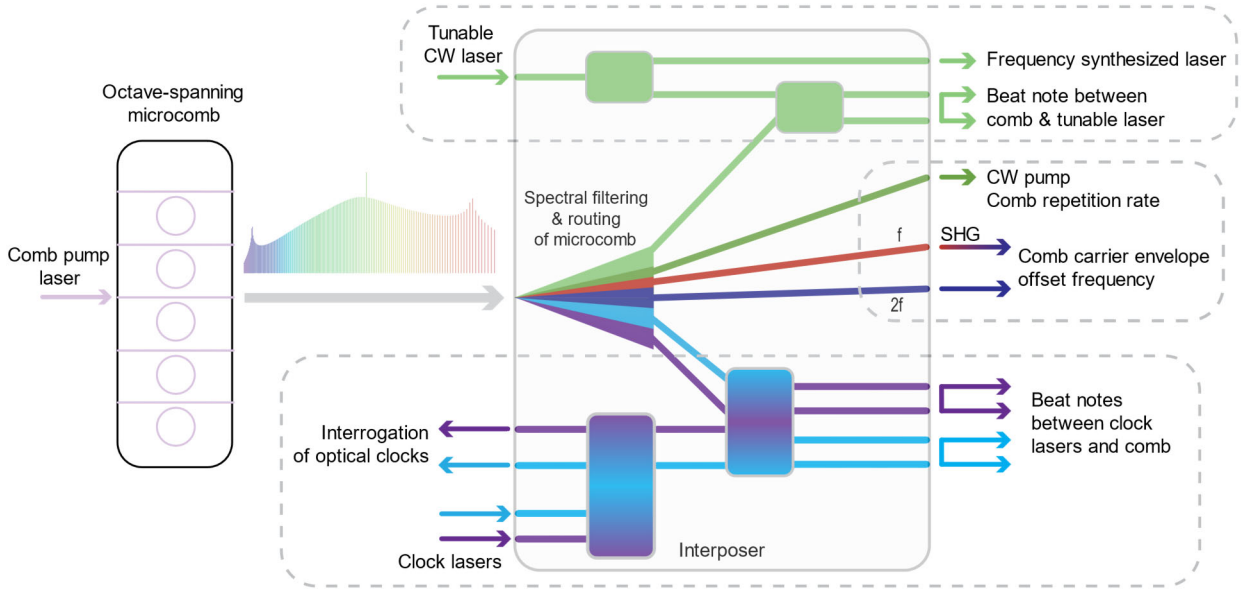

FIG. 1: **Concept of photonic interposers for integrated processing of microcombs.** Photonic interposers for fully integrated microcomb-based systems will need to interface multiple photonic devices, such as microcombs and other nonlinear elements, and lasers and photodetectors. The functions of such interposers can be broadly classified in two parts, first, the broadband spectral routing of microcombs, and second, the coherent mixing of specific filtered bands and teeth of the microcombs with additional external signals. The broadband spectral routing of microcombs includes separation of f and 2f components for self-referencing via second harmonic generation (SHG) and additional filtering for repetition rate detection, which together enable microcomb stabilization for metrological-grade applications. Depending on the application, further microcomb processing may be required, such as extraction of the pertinent comb reference-band for optical frequency synthesis, or of comb teeth matched to specific atomic transitions for optical clocks. These bands and teeth are subsequently mixed with tunable lasers and clock lasers for beat note detection for synthesis and timekeeping. In this work, we demonstrate individual passive components suitable for such an interposer for a dual-microcomb based optical frequency synthesizer and implement the requisite spectral filtering of an octave-spanning microcomb.

Figure 1 schematically depicts microcombs and other integrated photonic devices in the context of systems such as optical frequency synthesizers and optical atomic clocks. To transition to an integrated system from the table-top, numerous optical functions are required with the simultaneous operation of multiple photonic devices in lockstep. These functions nominally translate to different materials requirements - optical gain is required for lasers, $\chi^{(3)}$ nonlinearity for microcombs, $\chi^{(2)}$ nonlinearity for second harmonic generation, low linear loss for passives, and a high responsivity, low dark current material for photodetectors. To address this challenge of combining multiple material responses and platforms, one approach is to interface several chiplets of different photonic materials on a common carrier via chip-to-chip facet coupling, benefiting from the use of reliable well-established photonics and the ability to prequalify each photonic element prior to system assembly. Another approach is to integrate all functions and materials together on one main photonic chip, akin to heterogeneous integration, where the benefits inherent to having a system on a chip will come at the cost of the requisite research and development. Crucially, a judicious combination of chip-to-chip facet coupling and heterogeneous integration can balance the pragmatism of using discrete chiplets of well-established photonic elements with the benefits and cost of heterogeneously integrating multiple material systems together, using a photonic interposer to bind the system together.

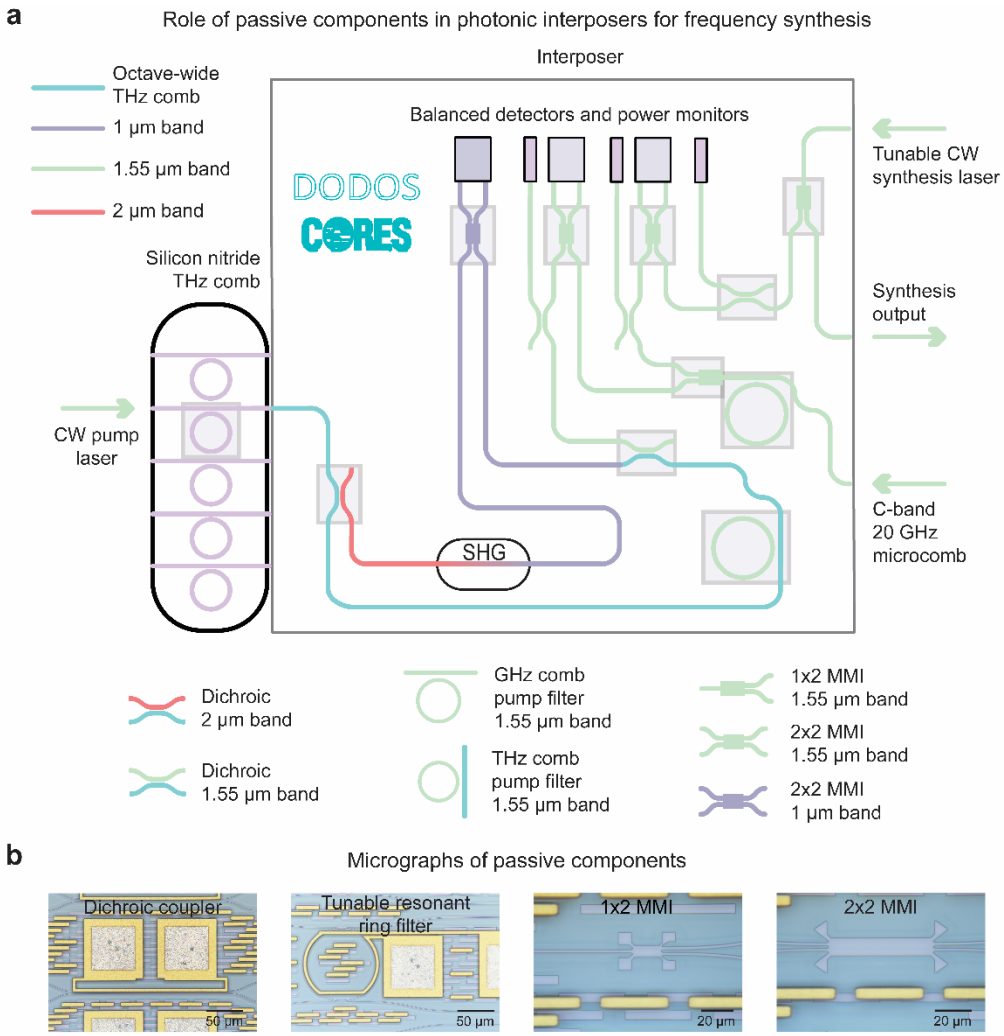

FIG. 2: **Envisioned role of passive components within a photonic interposer for a dual microcomb-based optical frequency synthesizer. a**. Conceptual schematic showing how the passive components demonstrated in this work (highlighted in light gray), octave-wide dichroics, tunable ring filters for microcomb pump extinction, and multimode interferometers, could fit into the proposed interposer and system architecture to form an integrated dual-microcomb based frequency synthesizer. The interposer is interfaced with THz repetition rate silicon nitride (also highlighted in light gray) and 20 GHz repetition rate silicon nitride or silica microcombs and a tunable laser via facet coupling, and with photodetectors and a second harmonic frequency doubler via heterogeneous integration. Dichroic directional couplers spectrally filter the silicon nitride microcomb in preparation for self-referencing and interference with the GHz microcomb for repetition rate stabilization. In turn, the output tunable frequency synthesis laser is referenced to the GHz microcomb. Multimode interferometers are utilized to generate these stabilization beat notes via balanced detection, and power monitors are used for additional system-level monitoring. Metal traces are not shown in this schematic. A detailed discussion showing the feasibility of such a system using only integrated components is included in the Supplementary Information (Notes 7 and 8). **b.** Micrographs of the individual interposer components shown in this work, dichroic directional couplers, ring resonator tunable filters, and multimode interferometers.

Figure 1 also indicates the nature of microcomb processing required of such photonic interposers. Spectral bands of combs generated in nonlinear resonators pumped by chip-scale lasers need to be adequately filtered across an octave bandwidth to facilitate stabilization via f-2f self-referencing, where additional nonlinear devices are required for the frequency doubling. Additionally, narrow spectral filtering of the strong pumps that drive the microcombs is required to prevent damage to and maintain the performance of both slow and fast photodetectors that monitor optical power and facilitate phase-locking via optical interference in on-chip coherent mixers. The approach upon which our interposer design is based uses two phase-stable interlocking Kerr combs to form the optical reference for synthesis[12], each pumped near 1550 nm, and generated in separate

silicon nitride (Si_3N_4) and Si_3N_4 or silica (SiO_2) microresonators with repetition rates of ≈ 1 THz and ≈ 20 GHz, respectively. The dual-microcomb system assists in reducing power consumption compared to a single octave-spanning microcomb of a directly detectable repetition rate, where the octave spanning Si_3N_4 comb is used for self-referencing and a narrower 20 GHz comb is used for repetition rate and synthesis frequency detection.

RESULTS

Interposer architecture

Figure 2a shows a schematic of the full photonic interposer design, which is based on transverse-electric (TE) polarized guided light in a 400 nm thick stoichiometric Si_3N_4 photonic platform with upper and lower silicon dioxide cladding. The Si_3N_4 platform is well established for numerous applications, and its low optical loss and high optical damage threshold, coupled with its broad optical transparency, assist in processing both low and high-power optical signals across the octave bandwidth. The nitride film thickness and waveguide widths are chosen to balance optical confinement, proximity to the optical single mode condition, and coupling to both heterogeneously integrated and facet-coupled elements, in contrast to microcombs where the anomalous dispersion required for octave spanning bright Kerr solitons necessitates films that are nearly a factor of two thicker. Further details regarding optical confinement and the number of modes can be found in the Supplementary Information (Note 1).

Interposer components

The passive components of the interposer are dichroic directional couplers (hereafter referred to as dichroics), resonant filters, 50:50 multimode interferometers (MMIs), and power splitters and taps that operate on the two microcombs and the tunable synthesis laser (Fig. 2b). These elements interface with a frequency doubler (SHG) including a polarization rotator, and a photodetector array that are heterogeneously integrated[33,39,42,52]. The output of the octave-spanning Si_3N_4 comb chip is directed to two cascaded dichroics that spectrally filter the microcomb into three key spectral bands, a long and a short wavelength band around 2 μm and 1 μm respectively, separated by an octave, and the center band around 1.55 μm. The first dichroic separates out light in the 2 μm band from shorter wavelengths, and the second dichroic separates 1.55 μm light from shorter wavelengths (in particular, the 1 μm light). The 2 μm light is led to the frequency doubler, after which the upconverted output in the 1 μm band is coherently mixed with the 1 μm microcomb light in a 2×2 50:50 MMI and detected to extract the carrier envelope offset frequency of the THz comb. Two 1×2 50:50 MMIs split the 20 GHz comb and the tunable synthesis laser (which reside on separate chips that are butt-coupled to the interposer). An additional 2×2 50:50 MMI is used to coherently mix the 20 GHz comb with the 1.55 μm band of the Si_3N_4 comb light, while a second 2×2 50:50 MMI mixes the 20 GHz comb with the tunable laser. The MMI outputs are used to phase-lock the two microcombs and detect the precise optical frequency of the tunable laser. In addition, two thermally tunable microring resonators filter out the microcomb pumps in the 1.55 μm band, and power taps and detectors are used to monitor the optical power of the microcombs and tunable laser. In the following three subsections, we first demonstrate the individual passive components of the interposer, i.e., MMIs, ring filters, and octave-wide dichroics. Our choice of the specific passive devices here is motivated by their specific application. In particular, we use ring filters to filter microcomb pumps because of the inherent vernier effect with the remainder of the microcomb that minimizes any undesired filtering of other microcomb tones, the ability to engineer microring-waveguide coupling across the wide spectral bands used here, and the capability to thermally tune the ring filters to precisely overlap the pump frequencies. Similarly, our choice of directional couplers for the dichroics is motivated by their inherent low loss and transmissive operation, along with the ability to design large bandwidths with high extinction ratios. We design these passive components employing a combination of waveguide eigenmode and 3D finite-difference time-domain (FDTD) simulations, and fabricate them on 100 mm wafers using process sequences based on both deep ultraviolet lithography (Ligentec) and electron-beam lithography (NIST). We validate our designs and fabrication by experimentally confirming the predicted component performance using both continuous-wave (CW) light and octave spanning microcomb light. Progress in the heterogeneously integrated interposer components, i.e., the frequency doubler and the photodetectors, has already been reported elsewhere[33, 39,42,52], we do not develop them further here. These components are discussed in depth in the context of a system-level analysis later in the Supplementary Information (Notes 7 and 8).

Multimode interferometers

Figure 3a shows 3D FDTD simulations of the 1×2 and 2×2 50:50 MMIs that function as power splitters and coherent mixers, respectively (see Methods and Supplementary Information Note 2 for details). The transmission ratio of the optical powers at the output ports of the 2×2 MMIs impact the balanced detection of the beat notes for phase-locking, motivating our choice of a butterfly multimode interferometer over a directional coupler. The corners of the butterfly geometry funnel out potential reflections that are deleterious to both the unity transmission ratio and the operation of an integrated circuit[53]. The corresponding CW transmission measurements of the bar and cross ports are shown in Fig. 3b for a range of MMI lengths, and the optimum MMI length agrees with our simulations. The excess loss, defined as transmission loss relative to the maximum transmission (nominally -3 dB), for all three optimal MMIs lengths is less than 0.5 dB, and includes variations from coupling on and off the chip.

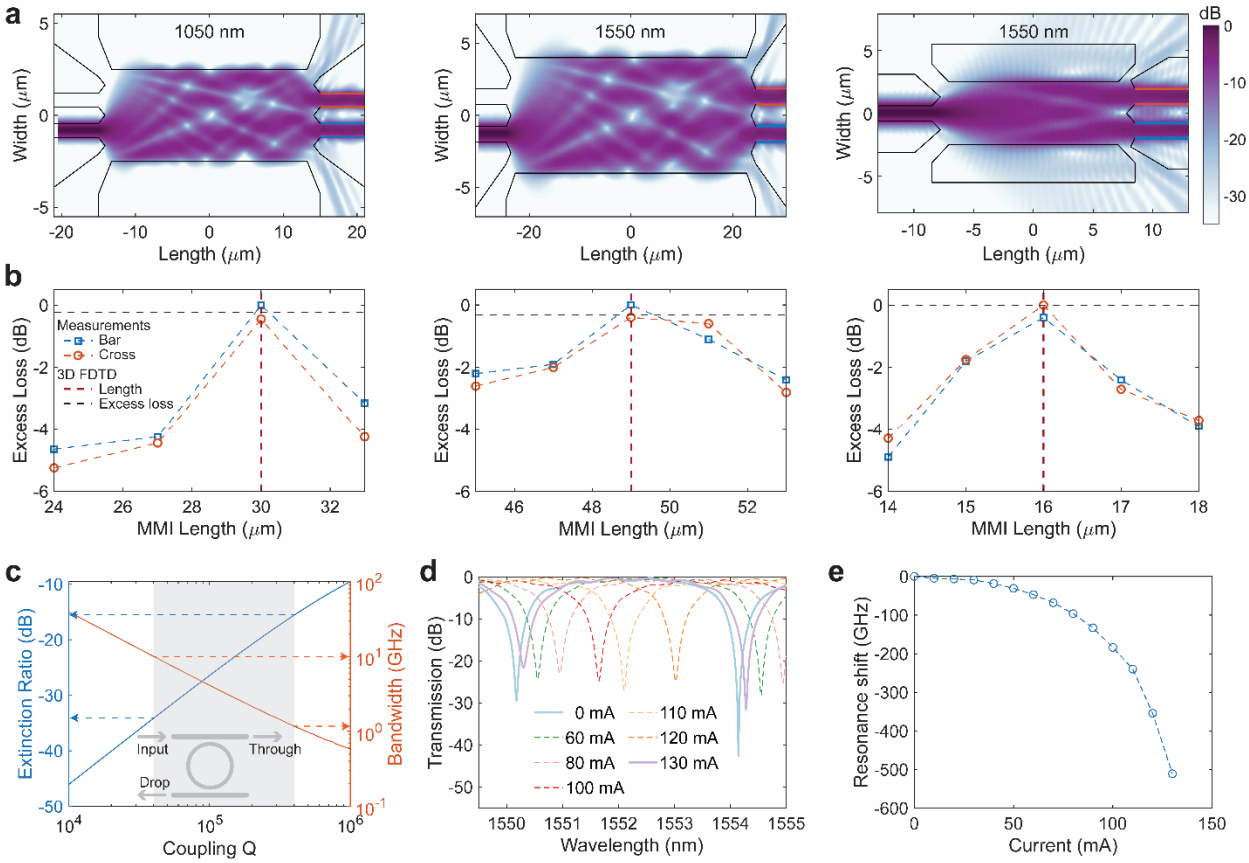

FIG. 3: **Multimode interferometers and microring filters. a.** Simulations showing the propagation of light from left to right in the three multimode interferometers at 1050 nm and 1550 nm. The corners of the butterfly geometry guide out light at the ≈ -25 dB level, suppressing potential reflections. The bar and cross output ports are highlighted in orange and blue outlines, respectively. Cross-sections of $|E(x,y,z)|^2$ are plotted with z set to half the height of the MMIs. **b.** Corresponding continuous-wave measurements of the bar and cross ports of the MMIs for a range of MMI lengths. In each case, the optimal MMI length matches the predicted length from the simulations in a. The associated measurement uncertainty is less than 0.2 dB based on one standard deviation in the transmission of five identical cascaded multimode interferometers. **c.** Simulated dependence of microring filter characteristics, extinction ratio and bandwidth, on coupling Q for an intrinsic Q of 10^6. Coupling Qs between 4×10^4 and 4×10^5 yield extinction ratios between 15 to 35 dB and corresponding filter bandwidths of 1 to 10 GHz, a range of filter characteristics suitable for our intended application of suppressing the pump of microcombs. **d.** Measured transmission spectra for a thermally tuned microring filter using an integrated heater. **e.** Variation of resonance frequency shift with heater current corresponding to **d**, showing over one free spectral range of tuning.

Microring filters

The filter bandwidth and extinction ratio of the thermally tunable symmetric add-drop microring filters that filter CW pump light are determined by the intrinsic and coupling quality factors (Q), which depend on absorption and scattering, and on the magnitude of coupling between the bus waveguide and the microring[54,55], respectively (Fig. 3c). Measurements (Fig. 3d and 3e) show that a ring filter with 50 μm radius (474.8 GHz free spectral range (FSR)) suitable for the Si_3N_4 microcomb (coupling Q ≈ 2×10^4, intrinsic Q ≈ 10^6 can be thermally tuned over 500 GHz, i.e., over an entire FSR, while maintaining adequate extinction, a requirement for matching the resonance of the filter with the pump of the Si_3N_4 microcomb. The maximum extinction measured, and variations therein, are limited by thermally induced perturbations to the coupling, and the polarization extinction ratio of the input light. For typical THz repetition rate microcombs, the pump power is 15 to 20 dB higher than the neighboring comb teeth. Therefore, to flatten the pump comb tooth to match the surrounding teeth, a coupling Q as high as ≈ 10^5 can be adequate. A similar microring with coupling Q ≈ 10^5 will be suitable for filtering the 20 GHz microcomb. Additional details regarding design and fabrication can be found in the Supplementary Information (Note 3) and the Methods. While our intended application requires moderate filtering and can take advantage of an inherent vernier effect between the filter and microcomb resonators, more demanding applications can use cascaded ring filters to synthesize more complex filter responses[56,57]. The 474.8 GHz ring filter FSR is sufficiently close to half of the microcomb's THz FSR for the vernier effect to ensure there is no spurious filtering of the THz microcomb in the C-band. Similarly, the 474.8 GHz FSR also provides a spurious-filtering free bandwidth of approximately 3.8 THz in the C-band for the 20 GHz microcomb.

Dichroic couplers

Figure 4a shows simulations for the dichroic that extracts the 2 μm microcomb band into the cross port. We measured the cross and bar port transmission for a range of directional coupler lengths using CW light at the three bands, and observed agreement with the expected optimized coupler length, with 15 dB of contrast at 2 μm and 1.55 μm, and over 30 dB at 1 μm, see the Supplementary Information (Note 4) for details. Figure 4b shows the measured individual bar and cross port spectra of the optimized dichroic across the nominal octave bandwidth centered around the telecom C band. The measurement uses an octave spanning Si_3N_4 microcomb (Fig. 4b, inset), generated in a 770 nm thick microring with low and broadband anomalous dispersion, as the input. Figure 4c compares the measured transmission with the simulated transmission, and magnified views of measurements in the 2 μm, 1.55 μm, and 1 μm bands are shown in Fig. 4d. Similarly, the second dichroic couples out the 1.55 μm microcomb light into the cross port, leaving the 1 μm band in the bar port, as seen in simulations at these wavelengths in Fig. 4e. Corresponding CW measurements indicated over 20 dB of contrast between the two ports, see the Supplementary Information (Note 4) for details. The behavior of this dichroic in the 2 μm band is inconsequential because it is intended to process the Si_3N_4 microcomb after the 2 μm band is filtered out in the first dichroic (Fig. 2). Figure 4f shows the measured individual bar and cross port spectra of the optimized dichroic, using the same microcomb input employed to evaluate the first dichroic (Fig. 4b, inset). Figure 4g compares the simulated and measured transmission of the dichroic across the octave, and magnified views of the spectral bands are shown in Fig. 4h. Overall, the performance of the two dichroics is appropriate for our intended application and largely follows the simulated behavior, with deviations observed only below the ≈ -20 dB level, likely originating from limitations of the measurement setup. Further details regarding design optimization and the experimental setup can be found in the Methods and Supplementary Information (Notes 4 and 6).

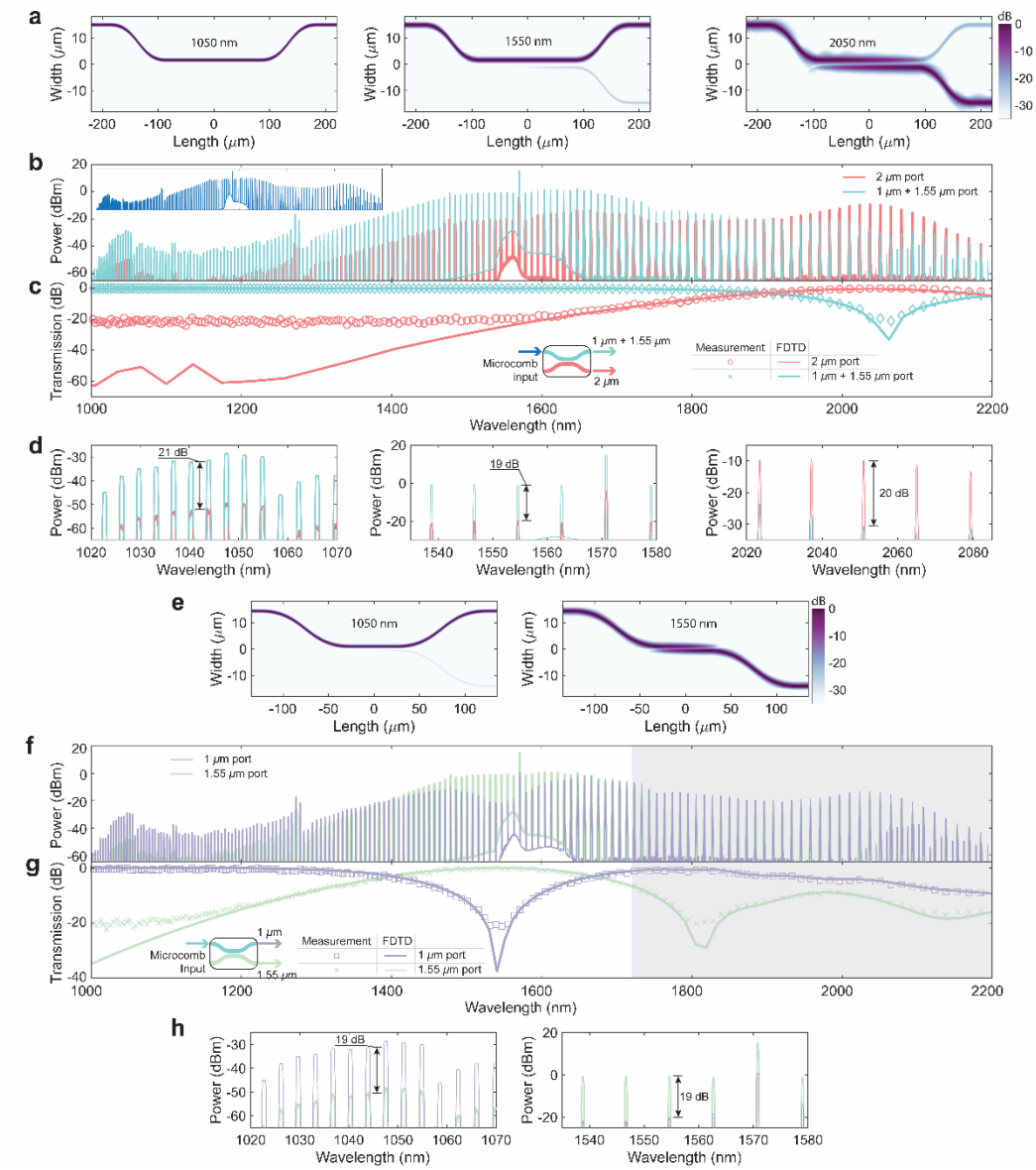

FIG. 4: **Octave wide operation of dichroics. a-d** First dichroic, whose purpose is to separate 2 μm light from shorter wavelengths. **a.** Simulations at 1050 nm, 1550 nm, and 2050 nm showing extraction of the 2 μm band into the cross port. **b.** Measured broadband experimental spectra at the bar and cross ports. The input is the microcomb shown in the inset. **c.** Measured (symbols) and simulated (solid lines) octave wide transfer function. At the cross or 2 μm port, extinction ratios of (21.4 ± 1.1) dB and (19.9 ± 0.8) dB are measured in the 1 μm and 1.55 μm bands, respectively. At the bar port, an extinction ratio of (18.1 ± 2.9) dB is measured in the 2 μm band. **d.** Magnified individual spectral bands. **e-h** Second dichroic, whose purpose is to separate 1.55 μm light from shorter wavelengths. **e.** Simulations at 1050 nm and 1550 nm, showing extraction of the 1.55 μm band into the cross port. **f.** Measured broadband experimental spectra at the bar and cross ports. The input is the microcomb shown in the inset of **b. g.** Measured (symbols) and simulated (solid lines) octave wide transfer function. At the cross or 1.55 μm port, an extinction ratio of (20.1 ± 1.0) dB is measured in the 1 μm band, and at the bar port, an extinction ratio of (18.6 ± 3.3) dB is measured in the 1.55 μm band. **h.** Magnified individual spectral bands. The performance of the dichroic in the spectral region shaded in **f** and **g** is relatively unimportant, as this region is filtered out by the first dichroic in the full interposer chip. In **a** and **e**, cross-sections of $|\mathbf{E}(x,y,z)|^2$ are plotted with z set to half the height of the dichroics. The measured transfer functions shown in **c** and **g** are extracted from the corresponding transmission of the comb teeth in **b** and **f**. The corresponding uncertainties reported in **c** and **g** correspond to line-to-line fluctuations in the measured comb spectra and include variations in coupling and are one standard deviation values.

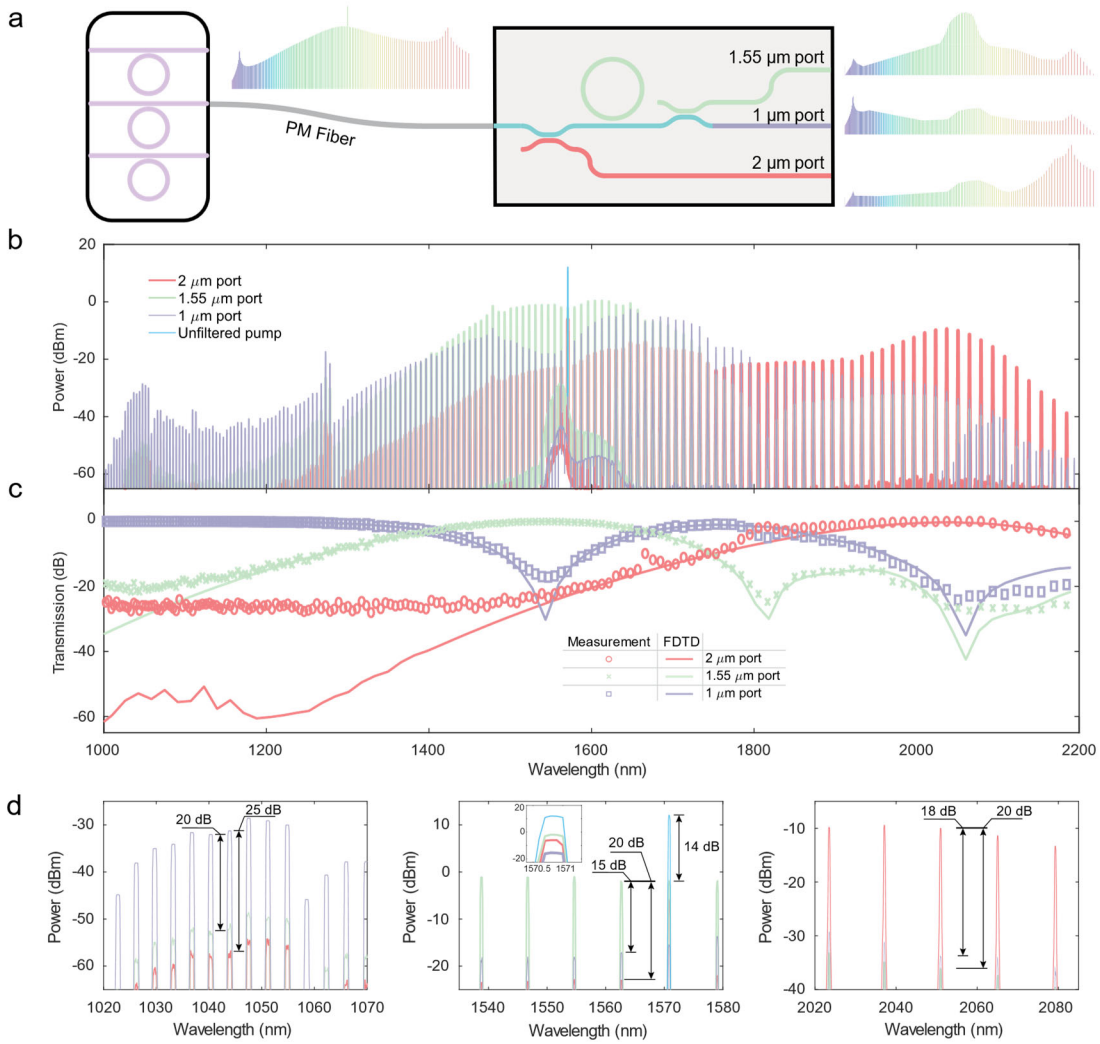

FIG. 5: **Integrated spectral processing of a microcomb. a.** Schematic for on-chip processing of a silicon nitride based octave spanning microcomb. PM = polarization maintaining. Here a PM fiber is used to link the two chips for convenience in testing, but finite element simulations suggest that direct facet-to-facet coupling with ~1 dB loss should be possible**. b.** Experimental spectra measured at the three output ports. The microcomb shown in the inset of Fig. 4b is used as the input. **c.** Measured (symbols) and simulated (solid lines) octave wide transfer functions. The measured transfer function is extracted from the transmission of the comb teeth in **b**. At the 1 μm port, extinction ratios of (16.2 ± 0.8) dB and (20.9 ± 2.2) dB are measured in the 1.55 μm and 2 μm bands, respectively. Similarly, at the 1.55 μm port, extinction ratios of (20.2 ± 0.7) dB and (25.6 ± 2.1) dB are measured in the 1 μm and 2 μm bands, and at the 2 μm port, extinction ratios of (26.1 ± 0.8) dB and (22.7 ± 0.9) dB are measured in the 1 μm and 1.55 μm bands. **d.** Magnified comparison of the outputs at the three ports in the individual spectral bands. Separation of the three spectral bands into the three ports with 15 dB to 25 dB of contrast is observable, along with 14 dB of pump suppression after comb generation from the ring filter (light blue comb tooth). The uncertainties reported in **c** correspond to line-to-line fluctuations in the comb spectra and include variations in coupling, and are one standard deviation values.

Integrated processing of an octave-spanning microcomb

So far, we have presented the design and experimental characterization of individual interposer elements. As a first demonstration of processing an octave spanning microcomb using a more integrated photonic chip that contains all of the aforementioned filtering capability, we measured the transmission through a chip comprised of a sequence of the two dichroics with a microring filter at the 1.55 μm band port (Fig. 5a), using an octave spanning microcomb (Fig. 4b, inset) as the input. Measurements shown in Fig. 5b show that the three spectral bands of interest are routed into the three physical ports. The ring filter reduces the pump amplitude to that of

the neighboring comb tones. Figure 5c compares the transfer function extracted from Fig. 5b to simulations based on 3D FDTD, excluding the effect of the ring filter that has no effect on the transmission envelope, showing good agreement between the two. Magnified views of the three spectral bands are shown in Fig. 5d. We observe 15 dB to 25 dB of extinction across the spectral bands at the outputs, along with 14 dB of pump suppression from the ring filter. Similar to the characterization of the individual dichroics, deviations occurring below the ≈ -20 dB level result from limitations of the measurement; see the Methods and Supplementary Information (Note 6) for more details regarding the fabrication and experimental setup.

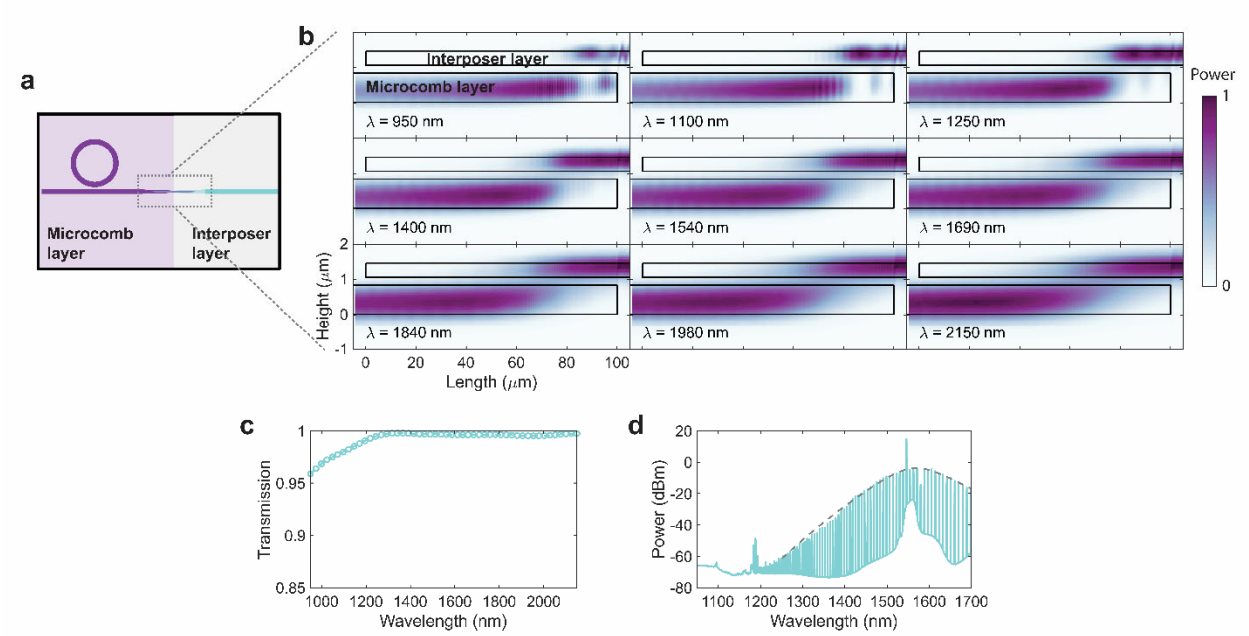

FIG. 6: **Towards microcomb-interposer integration. a.** Schematic showing integration of the microcomb and interposer photonics layers that are interfaced by a bilayer taper that can transfer an octave of comb bandwidth with negligible loss. **b,c.** Simulations of a 100 μm long bilayer taper showing low-loss broadband transfer of light. **d.** Broadband microcomb, along with the corresponding $sech^2$ fit, measured from a fabricated bilayer chip where the microcomb output is extracted through the bilayer taper into the interposer layer.

Towards microcomb-interposer integration

Looking forward, we show that our microcomb sources can be integrated with our photonic interposer layer, as envisioned in Fig. 6a. Bright Kerr soliton generation directly within the 400 nm thick Si_3N_4 interposer layer is not possible in conventional ring geometries due to the normal dispersion associated with all waveguide widths at that thickness. One could instead consider making the interposer out of a thicker Si_3N_4 layer (i.e., suitable for broadband anomalous dispersion), but the design of passive elements may be complicated by the increased confinement and larger numbers of modes supported by the thicker film. We instead adopt a dual layer approach, shown in Fig. 6. Here, fabrication of a thick Si_3N_4 layer (the microcomb layer) is followed by a vertically coupled thin Si_3N_4 layer (the interposer layer), with chemical-mechanical polishing enabling control of the SiO_2 film thickness separating the layers. A key challenge for this approach is the transfer of the microcomb to the interposer layer across a full octave of bandwidth. We address this challenge by using a 100 μm bilayer taper (schematic top-view shown in Fig. 6a) that ensures adiabatic transfer of light with less than 1 dB of loss across an octave, simulated using 3D FDTD (Fig. 6b and 6c). The Si_3N_4 film thicknesses of the microcomb and interposer layers are 790 nm (a common thickness for broadband combs[17,26]) and 400 nm, respectively, with an interlayer SiO_2 thickness of 200 nm (see Supplementary Information Note 5 for details). Both layers are tapered in width from 1 μm to 0.2 μm over a 100 μm length. Importantly, the adiabatic nature of the taper is such that it is relatively insensitive to precise interlayer SiO_2 thickness (at the 50 nm level), as well as lateral offsets between the waveguide layers (at the 100 nm level). Figure 6d shows a Kerr soliton microcomb generated in a ring of 23 μm radius, measured after transfer through the bilayer taper. No spectral

degradation was observed in comparison to a microcomb pumped in the opposite direction, where the microcomb does not pass through the bilayer taper. The reduced bandwidth of the microcomb compared to that used previously in this work precludes its use in the demonstration shown in Fig 5, and stems from differences in dispersion that primarily arise from the different Si_3N_4 thickness used (790 nm targeted here vs. 770 nm previously). Nevertheless, this serves as a conclusive demonstration that the thick Si_3N_4 layer associated with microcomb generation can be integrated on the same chip with thinner Si_3N_4 that is preferable for linear functionality.

DISCUSSION

Different approaches have been established in the literature for integrated dichroic filtering. These include the use of symmetric and asymmetric directional couplers[58-60], asymmetric Y-junctions[61-63], sub-wavelength gratings[64,65] and photonic crystals[66], multimode interferometers[67,68], Mach-Zehnder interferometers[69] and optical lattice filters[70], and inverse designed structures[71], on popular photonics platforms. Of these, the directional coupler-based approach is well-suited for broadband applications such as ours here, having shown a combination of good extinction ratios, high bandwidths, low loss, and transmissive operation. Most pertinent to our work, bandwidths of over two-thirds of an octave[58] and over an octave[59], both centered around 1.55 μm, have been demonstrated, accompanied by losses varying between 0.5 dB to 3 dB and extinction ratios between 11 dB and 30 dB across the different bands of operation. Our dichroics, also based on directional couplers, are demonstrated over an octave of bandwidth, with losses < 0.25 dB (measurements limited by variations in fiber coupling) and extinction ratios of 16 dB to 26 dB in the three pertinent bands (1 μm, 1.55 μm, and 2 μm). The performance offered by our other interposer components, MMIs and ring filters, is commensurate with the current state of the art in silicon nitride photonics[72-77], where 0.5 dB of excess MMI loss, similar to our MMIs, and microring filters with intrinsic Qs around 10^6 and extinction ratios in excess of 20 dB and 80 dB for first and third order filters have been reported. For the case of the ring filters, the utility of intrinsic Q and maximum extinction ratio are strongly application dependent – for our application, we engineer the coupling Q to ensure strong undercoupling and overcoupling only up to a desired extent in the 1 μm and 1.55 μm bands, respectively. In the context of our bilayer taper microcomb source, much progress has been realized in multiplanar photonics using combinations of different photonic materials[29-33,39-42], particularly in nonlinear photonics. Notably, linear high Q silicon nitride resonators have been previously integrated with silicon bus waveguides[78]. In relation to our proposed scheme here (Fig. 2), III-V-based SHG and photodetectors have been shown on insulator and 400 nm thick silicon nitride[33,39,42].

We perform a numerical analysis to confirm the feasibility of the synthesizer proposed in Fig. 2. The signal-to-noise ratios (SNRs) of the three beat notes measured between the 2f and frequency doubled f tones of the THz microcomb for the carrier envelope offset frequency (f_{CEO}) and self-referencing, between the dual microcombs for interlocking, and between the synthesis laser and the 20 GHz microcomb are key to the performance of such a system. The two beat notes of the dual-microcombs and the synthesis laser-20 GHz microcomb lie within the nominal bandwidth for heterogeneously integrated photodetectors on Si_3N_4[33]. However, the carrier envelope offset frequency (f_{CEO}) beat note for self-referencing of the THz microcomb can in principle vary between -500 GHz and +500 GHz (the repetition rate). By judicious tuning of the microring geometry, one can simultaneously achieve dual-dispersive waves at f and 2f frequencies along with the pinning of f_{CEO} to within the photodetector bandwidth. In particular, the microcomb dispersion is largely dominated by the microring cross-section (ring width and height), while the ring radius has comparatively minimal impact on the dispersion and therefore, appropriate choice of ring radius keeps f_{CEO} in a detectable range. Further details, including strategies for managing the f_{CEO} range for the bilayer integration approach indicated in Fig. 6, can be found in the Supplementary Information (Note 8.1). In addition to interposer component performance, the beat note SNRs are determined by a combination of other photonics and electronics–related factors, such as chip laser power, microcomb performance, SHG efficiency, photodetector responsivity and bandwidth, transimpedance amplifier (TIA) performance, coupling efficiencies, and transmission loss throughout the system, and locking electronics. The Supplementary Information (Notes 7 and 8) offers a detailed discussion of the proposed system (using a silica microcomb for the 20 GHz comb), including the distribution of power throughout it, the impact of the aforementioned factors including interposer component performance, and the final SNRs of the three beat notes. We find that using a conservative analysis based on device performances corresponding to contemporary demonstrations and realistic system operation, we estimate the beat note SNRs as 16.9 to 25.5

dB, 25 dB, and 31.1 dB for f_{CEO}, the dual-microcomb lock, and the synthesis laser-silica microcomb lock, adequate for system operation. Furthermore, improvements over the current performance of the interposer components shown here are seen to offer minimal improvement in the beat note SNRs; an analysis of the impact of dichroic extinction ratios and MMI excess losses is included in the Supplementary Information (Note 8.9).

In summary, we have demonstrated octave-wide dichroic filters, multimode interferometers, and tunable ring filters in the silicon nitride photonic platform. These passive elements are envisioned to be the core ingredients in a future integrated photonics interposer architecture for a microcomb-based optical frequency synthesizer that uses a variety of photonic devices to collect, route, and interface broadband light from discrete chiplets and heterogeneously integrated photonic devices. Such an architecture is important for addressing a key impediment in the full chip-scale integration of multiple material systems and functional responses for microcomb-based systems. We use the well-known Si_3N_4 photonic platform because of its low absorption, high damage threshold, and broad optical transparency, and validate our approach with a combination of electromagnetic calculations and measurements on fabricated devices integral to the interposer. We perform a series of short-loop tests where our designs for dichroic couplers, resonant filters, and multimode interferometers show experimental performance well-suited for processing microcombs, in congruence with our simulations. In addition to measurements using continuous-wave inputs, we use an octave-spanning microcomb generated in a thick silicon nitride chip as the input to directly confirm the ability of the dichroic couplers to process octave-wide light. Following the success of the individual interposer elements, we demonstrate octave-wide spectral processing of an octave-spanning microcomb through an integrated chain of two dichroic couplers and a ring filter which constitute the key broadband comb processing sequence of the interposer, and measure the expected spectral contrast in the wavelength bands of interest, along with the flattening of the pump tone to match the remainder of the microcomb. Further, we report the single-chip integration of a broadband Si_3N_4 microcomb with the Si_3N_4 photonic layer used for the interposer components by using a broadband adiabatic taper to transfer the microcomb output between the thick microcomb and thinner interposer layers, indicating a path towards integrating microcombs with additional customizable photonic processing. Finally, we numerically analyze the potential performance of the proposed integrated photonics synthesizer architecture in light of the demonstrated component-level performance. The interposer components we have developed can be adapted to develop interposer architectures for other microcomb-based integrated systems for optical atomic clocks, high-precision spectroscopy, and precise navigation, among others, based on similar requirements for microcomb-processing and system integration.

MATERIALS AND METHODS

Device Designs

The devices are designed using a combination of eigenmode simulations, coupled mode theory, and 3D finite difference time domain simulations. Waveguide modes, microring modes, and effective indices are simulated across an octave bandwidth using COMSOL. Coupling coefficients between identical straight waveguides are determined through supermode simulations and the coupling between microrings and straight bus waveguides is calculated using coupled mode theory. The propagation of light and related transmission transfer functions shown in Figs. 4–6 are extracted from octave-wide 3D finite difference time domain simulations.

Device Fabrication

All devices used here are fabricated on silicon dioxide (SiO_2)-clad silicon nitride (Si_3N_4) photonic platforms. Low pressure chemical vapor deposition is used to deposit these Si_3N_4 layers. The Nanolithography Toolbox, a free package developed by the NIST Center for Nanoscale Science and Technology, was used for all device layouts. Broadband ellipsometry was used along with an extended Sellmeier model to evaluate the refractive index across the wavelength range of interest. All devices are fabricated on 100 mm silicon wafers. The octave spanning microcomb, the interposer elements (multimode interferometers, ring filters, and dichroics), and the bilayer microcomb are fabricated at Ligentec using deep-UV lithography. All of these are patterned via reactive ion etching, except for the microcomb layer of the bilayer microcomb, which is patterned using a damascene process. The integrated microcomb spectral filter is fabricated at NIST using electron-beam lithography and reactive ion etching.

ACKNOWLEDGEMENTS

We gratefully acknowledge support by the Defense Advanced Research Projects Agency (DARPA-DODOS), NIST-University of Maryland (70NANB10H193), and National Institute of Standards and Technology (NIST-on-a-chip). A.R. and X.L. gratefully acknowledge support under the Cooperative Research Agreement between the University of Maryland and NIST-CNST, Award no. 70NANB10H193.

CONFLICT OF INTERESTS

The authors declare that they have no conflict of interests.

CONTRIBUTIONS

A.R., G.M. and K.S. carried out device design. A.R., D.A.W., D.S., M.G. and M.Z. performed device fabrication. A.R., and G.M. conducted measurements with assistance from X.L. and K.S. All authors participated in the analysis and discussion of the results. A.R. and K.S. wrote the manuscript with assistance from all authors. S.B.P., J.B. and K.S. supervised the project.

REFERENCES

1. S. T. Cundiff and J. Ye, "Colloquium: Femtosecond optical frequency combs," Rev. Mod. Phys. **75**, 325–342 (2003).
2. T. J. Kippenberg, A. L. Gaeta, M. Lipson, and M. L. Gorodetsky, "Dissipative Kerr solitons in optical microresonators," Science **361**, eaan8083 (2018).
3. A. L. Gaeta, M. Lipson, and T. J. Kippenberg, "Photonic-chip-based frequency combs," Nat. Photonics **13**, 158–169 (2019).
4. A. Pasquazi et al, "Micro-combs: A novel generation of optical sources," Phys. Reports **729**, 1–81 (2018).
5. G. Moille, Q. Li, S. Kim, D. Westly, and K. Srinivasan, "Phased-locked two-color single soliton microcombs in dispersion-engineered Si_3N_4 resonators," Opt. Lett. **43**, 2772–2775 (2018).
6. J. Yang et al, "Coherent satellites in multispectral regenerative frequency microcombs," Commun. Phys. **3**, no. 27 (2020).
7. Y. Zhao et al, "Visible nonlinear photonics via high-order-mode dispersion engineering," Optica **7**, 135–141 (2020).
8. S.-P. Yu et al, "Spontaneous Pulse Formation in Edge-Less Photonic Crystal Resonators," arXiv:200212502 (2020).
9. A. Tikan et al, "Emergent Nonlinear Phenomena in a Driven Dissipative Photonic Dimer," arXiv:200506470 (2020).
10. D. J. Jones et al, "Carrier-envelope phase control of femtosecond mode-locked lasers and direct optical frequency synthesis," Science **288**, 635–639 (2000).
11. R. Holzwarth et al, "Optical frequency synthesizer for precision spectroscopy," Phys. Rev. Lett. **85**, 2264–2267 (2000).
12. D. T. Spencer et al, "An optical-frequency synthesizer using integrated photonics," Nature **557**, 81–85 (2018).
13. S. A. Diddams et al, "An optical clock based on a single trapped 199 Hg+ ion," Science **293**, 825–828 (2001).
14. Z. L. Newman et al, "Architecture for the photonic integration of an optical atomic clock," Optica **6**, 680–685 (2019).
15. W. C. Swann and N. R. Newbury, "Frequency-resolved coherent lidar using a femtosecond fiber laser," Opt. Lett. **31**, 826–828 (2006).
16. M. G. Suh and K. J. Vahala, "Soliton microcomb range measurement," Science **359**, 884–887 (2018).
17. J. Riemensberger et al, "Massively parallel coherent laser ranging using a soliton microcomb," Nature **581**, 164–170 (2020).
18. M. J. Thorpe, K. D. Moll, J. R. Jones, B. Safdi, and J. Ye, "Broadband cavity ringdown spectroscopy for sensitive and rapid molecular defection," Science **311**, 1595–1599 (2006).
19. M. G. Suh, Q. F. Yang, K. Y. Yang, X. Yi, and K. J. Vahala, "Microresonator soliton dual-comb spectroscopy," Science **354**, 600–603 (2016).
20. A. Dutt et al, "On-chip dual-comb source for spectroscopy," Sci. Adv. **4**, e1701858 (2018).
21. T. M. Fortier et al, "Generation of ultrastable microwaves via optical frequency division," Nat. Photonics **5**, 425–429 (2011).
22. J. Wu et al, "RF Photonics: An Optical Microcombs' Perspective," IEEE J. Sel. Top. Quantum Electron. **24**, no. 6101020 (2018).
23. E. Lucas et al, "Ultralow-noise photonic microwave synthesis using a soliton microcomb-based transfer oscillator," Nat. Commun. **11**, no. 374 (2020).
24. C. H. Li et al, "A laser frequency comb that enables radial velocity measurements with a precision of 1 cm s^{-1}," Nature **452**, 610–612 (2008).
25. A. J. Metcalf et al, "Stellar spectroscopy in the near-infrared with a laser frequency comb," Optica **6**, 233–239 (2019).

26. P. Marin-Palomo et al, "Microresonator-based solitons for massively parallel coherent optical communications," Nature **546**, 274–279 (2017).
27. A. Fülöp et al, "High-order coherent communications using mode-locked dark-pulse Kerr combs from microresonators," Nat. Commun. **9**, no. 1598 (2018).
28. B. Corcoran et al, "Ultra-dense optical data transmission over standard fibre with a single chip source," Nat. Commun. **11**, no. 2568 (2020).
29. N. Li et al, "Monolithically integrated erbium-doped tunable laser on a CMOS-compatible silicon photonics platform," Opt. Express **26**, 16200–16211 (2018).
30. K. Shtyrkova et al, "Integrated CMOS-compatible Q-switched mode-locked lasers at 1900nm with an on-chip artificial saturable absorber," Opt. Express **27**, 3542–3556 (2019).
31. D. Huang et al, "High-power sub-kHz linewidth lasers fully integrated on silicon," Optica **6**, 745–752 (2019).
32. A. Bhardwaj et al, "A Monolithically Integrated Racetrack Colliding-Pulse Mode-Locked Laser with Pulse-Picking Modulator," IEEE J. Quantum Electron. **56**, 2000708 (2020).
33. Q. Yu et al, "Heterogeneous photodiodes on silicon nitride waveguides," Opt. Express **28**, 14824–14830 (2020).
34. J. Lu et al, "Periodically poled thin-film lithium niobate microring resonators with a second-harmonic generation efficiency of 250,000%/W," Optica **6**, 1455–1460 (2019).
35. A. W. Bruch et al, "Pockels Soliton Microcomb," arXiv:200407708 (2020).
36. D. D. Hickstein et al, "Quasi-Phase-Matched Supercontinuum Generation in Photonic Waveguides," Phys. Rev.Lett. **120**, 053903 (2018).
37. N. Singh et al, "Octave-spanning coherent supercontinuum generation in silicon on insulator from 1.06 μm to beyond 2.4 μm," Light. Sci. Appl. **7**, no. 17131 (2018).
38. A. Rao et al, "Actively-monitored periodic-poling in thin-film lithium niobate photonic waveguides with ultrahigh nonlinear conversion efficiency of 4600 $\%W^{-1}cm^{-2}$," Opt. Express **27**, 25920–25930 (2019).
39. E. J. Stanton et al, "Efficient second harmonic generation in nanophotonic GaAs-on-insulator waveguides," Opt. Express **28**, 9521–9532 (2020).
40. L. Chang et al, "Heterogeneous integration of lithium niobate and silicon nitride waveguides for wafer-scale photonic integrated circuits on silicon," Opt. Lett. **42**, 803–806 (2017).
41. A. Honardoost et al, "Cascaded Integration of Optical Waveguides with Third-Order Nonlinearity with Lithium Niobate Waveguides on Silicon Substrates," IEEE Photonics J. **10**, no. 4500909 (2018).
42. E. J. Stanton et al, "On-chip polarization rotator for type I second harmonic generation," APL Photonics **4**, no. 126105 (2019).
43. B. Stern, X. Ji, Y. Okawachi, A. L. Gaeta, and M. Lipson, "Battery-operated integrated frequency comb generator," Nature **562**, 401–405 (2018).
44. A. S. Raja et al, "Electrically pumped photonic integrated soliton microcomb," Nat. Commun. **10**, 680 (2019).
45. B. Shen et al, "Integrated turnkey soliton microcombs," Nature **582**, 365–369 (2020).
46. J. L. Hall, "Nobel lecture: Defining and measuring optical frequencies," Rev. Mod. Phys. **78**, 1279–1295 (2006).
47. S. W. Huang et al, "A broadband chip-scale optical frequency synthesizer at 2.7×10−16 relative uncertainty," Sci. Adv. **2**, e1501489 (2016).
48. S. Arafin et al, "Power-Efficient Kerr Frequency Comb Based Tunable Optical Source," IEEE Photonics J. **9**, no. 6600814 (2017).
49. S. Arafin et al, "Towards chip-scale optical frequency synthesis based on optical heterodyne phase-locked loop," Opt. Express **25**, 681–695 (2017).
50. M. Xin et al, "Optical frequency synthesizer with an integrated erbium tunable laser," Light. Sci. Appl. **8**, no. 122 (2019).
51. N. Singh et al, "Silicon Photonics Optical Frequency Synthesizer," Laser Photonics Rev. **14**, 1900449 (2020).
52. R. Costanzo and S. M. Bowers, "A 10-GHz Bandwidth Transimpedance Amplifier with Input DC Photocurrent Compensation Loop," IEEE Microw. Wirel. Components Lett. **30**, 673–676 (2020).
53. E. Kleijn et al, "Multimode interference couplers with reduced parasitic reflections," IEEE Photonics Technol. Lett. **26**, 408–410 (2014).
54. C. Manolatou et al, "Coupling of modes analysis of resonant channel add-drop filters," IEEE J. Quantum Electron. **35**, 1322–1331 (1999).
55. G. Moille et al, "Broadband resonator-waveguide coupling for efficient extraction of octave-spanning microcombs," Opt. Lett. **44**, 4737–4740(2019).
56. T. Barwicz et al, "Microring-resonator-based add-drop filters in SiN: fabrication and analysis," Opt. Express **12**, 1437–1442 (2004).

57. R. Amatya, C. W. Holzwarth, H. I. Smith, and R. J. Ram, “Precision tunable silicon compatible microring filters,” IEEE Photonics Technol. Lett. **20**, 1739–1741 (2008).
58. T. Su et al, “A 2/3-Octave-Spanning Three Spectral Band Splitter on a Si_3N_4 Photonic Integrated Circuit Platform,” in Conference on Lasers and Electro-Optics, OSA Technical Digest (online) (Optical Society of America, 2017), paper SF1H.7.
59. E. J. Stanton, M. J. R. Heck, J. Bovington, A. Spott, and J. E. Bowers, “Multi-octave spectral beam combiner on ultra-broadband photonic integrated circuit platform,” Opt. Express **23**, 11272–11283 (2015).
60. E. S. Magden et al, “Transmissive silicon photonic dichroic filters with spectrally selective waveguides,” Nat. Commun. **9**, 3009 (2018).
61. T. Negami, H. Haga, and S. Yamamoto, “Guided-wave optical wavelength demultiplexer using an asymmetric Y junction,” Appl. Phys. Lett. **54**, 1080–1082 (1989).
62. Y. Shani, C. H. Henry, R. C. Kistler, R. F. Kazarinov, and K. J. Orlowsky, “Integrated optic adiabatic devices on silicon,” IEEE J. Quantum Electron. **27**, 556–566 (1991).,
63. M. H. Al-Gaf and D. Khalil, "FTTH triplexer design using asymmetric y-junction with etched branch," IEEE Photon. Technol. Lett. **19**, 1157–1159 (2007).
64. Z. Weissman, D. Nir, S. Ruschin and A. Hardy, “Asymmetric Y-junction wavelength de-multiplexer based on segmented waveguides,” Appl. Phys. Lett. **67**, 302–304 (1995).
65. D. Bucci, J. Grelin, E. Ghibaudo, and J.-E. Broquin, “Realization of a 980-nm/1550-nm pump-signal (de) multiplexer made by ion-exchange on glass using a segmented asymmetric y-junction,” IEEE Photon. Technol. Lett. **19**, 698–700 (2007).
66. J. S. Foresi et al, “Photonic-bandgap microcavities in optical waveguides,” Nature **390**, 143–145 (1997).
67. S. Singh et al, “An MMI-based wavelength combiner employing non-uniform refractive index distribution,” Opt. Express **22**, 8533–8540 (2014).
68. J. Mu, S. A. Vázquez-Córdova, M. A. Sefunc, Y.-S. Yong, and S. M. García-Blanco, “A Low-Loss and Broadband MMI-Based Multi/Demultiplexer in Si3N4/SiO2 Technology,” J. Lightwave Technol. **34**, 3603–3609 (2016).
69. G. Zhang, S. Honkanen, A. Tervonen, C.-M. Wu, and S. I. Najafi, “Glass integrated optics circuit for 1.48/1.55-and 1.30/1.55-μm-wavelength division multiplexing and 1/8 splitting,” Appl. Opt. **33**, 3371–3374 (1994).
70. S. Ibrahim et al, “Demonstration of a fast-reconfigurable silicon CMOS optical lattice filter,” Opt. Express **19**, 13245-13256 (2011).
71. A. Y. Piggott et al, “Inverse design and demonstration of a compact and broadband on-chip wavelength demultiplexer,” Nat. Photonics **9**, 374–377 (2015).
72. P. Muñoz et al, “Silicon nitride photonic integration platforms for visible, near-infrared and mid-infrared applications,” Sensors **17**, 2088 (2017).
73. C. G. H. Roeloffzen et al, “Low-Loss Si3N4 TriPleX Optical Waveguides: Technology and Applications Overview,” IEEE J. Sel. Top. Quantum Electron. **24**, 4400321 (2018).
74. D. J. Blumenthal, R. Heideman, D. Geuzebroek, A. Leinse, and C. Roeloffzen, “Silicon nitride in silicon photonics,” Proc. IEEE **106**, 2209–2231 (2018).
75. P. Munoz et al, “Foundry developments toward silicon nitride photonics from visible to the mid-infrared,” IEEE J. Sel. Top. Quantum Electron. **25**, 8200513 (2019).
76. C. Sorace-Agaskar et al, “Versatile silicon nitride and alumina integrated photonic platforms for the ultraviolet to short-wave infrared," IEEE J. Sel. Top. Quantum Electron. **25**, 1–15 (2019).
77. X. Hu et al, “Si_3N_4 photonic integration platform at 1 μm for optical interconnects,” Opt. Express **28**, 13019-13031 (2020).
78. Q. Li et al, “Vertical integration of high-Q silicon nitride microresonators into silicon-on-insulator platform,” Opt. Express **21**, 18236-18248 (2013).

Supplementary Information for

Towards integrated photonic interposers for processing octave-spanning microresonator frequency combs

Ashutosh Rao,[1,2,*] Gregory Moille,[1,3] Xiyuan Lu,[1,2] Daron A. Westly,[1] Davide Sacchetto,[4] Michael Geiselmann,[4] Michael Zervas,[4] Scott B. Papp,[5,6] John Bowers,[7] and Kartik Srinivasan[1,3,†]

[1]*Microsystems and Nanotechnology Division, Physical Measurement Laboratory, National Institute of Standards and Technology, Gaithersburg, MD 20899, USA*

[2]*Maryland NanoCenter, University of Maryland, College Park, MD 20742, USA*

[3]*Joint Quantum Institute, NIST/University of Maryland, College Park, MD 20742, USA*

[4]*Ligentec, EPFL Innovation Park, Batiment C, Lausanne, Switzerland*

[5]*Time and Frequency Division, Physical Measurement Laboratory, National Institute of Standards and Technology, Boulder, CO 80305, USA*

[6]*Department of Physics, University of Colorado, Boulder, CO 80309, USA*

[7]*Department of Electrical and Computer Engineering, University of California, Santa Barbara, CA 93106, USA*

*Email: ashutosh.rao@nist.gov

†Email: kartik.srinivasan@nist.gov

Note 1: Photonic platform

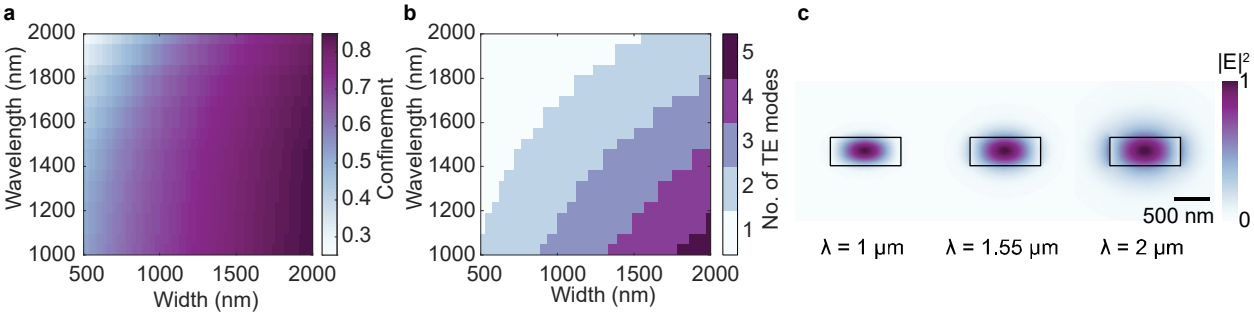

Fig. S1: **Photonics Platform. a,b.** Optical confinement and number of modes for channel waveguides in a 400 nm thick silicon nitride film with silicon dioxide upper and lower cladding. The optical confinement here is defined as h = $(\iint_{\text{core}} |\mathbf{E}(x,y)|^2\, dxdy)/(\iint |\mathbf{E}(x,y)|^2\, dxdy)$. A nominal waveguide width of 1 μm balances the confinement and number of modes across the octave, and is followed by additional tapering throughout the interposer to reach the target dimensions of specific elements (e.g., the dichroics). **c.** Waveguide transverse electric field modes simulated for wavelengths of 1 μm, 1.55 μm, and 2 μm, for a waveguide width of 1 μm. In keeping with **b**, $|\mathbf{E}(x,y)|^2$ is plotted.

Figures S1a and S1b show the variation of modal confinement of the fundamental transverse-electric (TE) mode and the number of TE modes with wavelength and waveguide width. Figure S1c shows simulated TE eigenmodes for a waveguide width of 1 μm that nominally balances these criteria. In selecting a photonic platform suitable for the proposed interposer, there are a few considerations that arise. The first is the ability to form the desired ring filters with free spectral ranges (FSRs) a little under 0.5 THz. This is related to the bending radius and optical confinement. The second is the efficiency of chip-to-chip coupling onto the interposer chip from lasers and microcomb chips. Finally, there is the footprint of the overall interposer, which is nominally limited by the heterogeneously integrated devices. In particular, for applications where 0.5 THz FSR ring filters are not essential, one can consider the use of low loss low-confinement nitride platforms where the core is approximately 100 nm thick and the optical mode significantly extends into the oxide cladding[1]. However, the microcomb pump filters here preclude our use of such a platform. Balancing the efficiency of chip-to-chip coupling with the other factors needs to be looked at on a case-by-case basis. Our use of a 400 nm thick silicon nitride film for the interposer devices and layer is suited to our proposed system. The use of other components and material systems may lead to a different optimal thickness. There are three instances of chip-to-chip coupling that occur into the proposed interposer (Fig. 2 of the main text and Fig. S8), with estimated coupling losses of < 1 dB across the octave from the THz microcomb chip, and <1 dB in the C-band from the GHz microcomb chip and the tunable laser chip, based on the mode overlaps. Here, the microcomb layer is 770 nm thick and can vary between 200 nm to 300 nm width at the facet using an oxide-clad inverse taper. The GHz microcomb consists of a silica microcomb coupled to a silicon nitride bus waveguide[2] (250 nm by 900 nm at the facet, no top oxide cladding), and the tunable laser is based on the heterogeneous integration of III-Vs onto silicon-on-insulator[3] (half-etched 500 nm by 5 μm oxide-clad ridge silicon cross section at the facet). Using a thicker device layer for the interposer will marginally increase coupling to the THz microcomb in practice but at the cost of decreasing the coupling to the GHz microcomb and tunable laser.

Note 2: Multimode interferometers

Figure S2 and Table S1 show the optimized design parameters of the multimode interferometers. Initial designs for a standard geometry[4] were adapted and optimized for the butterfly geometry[5] used here through 3D finite difference time domain (FDTD) simulations.

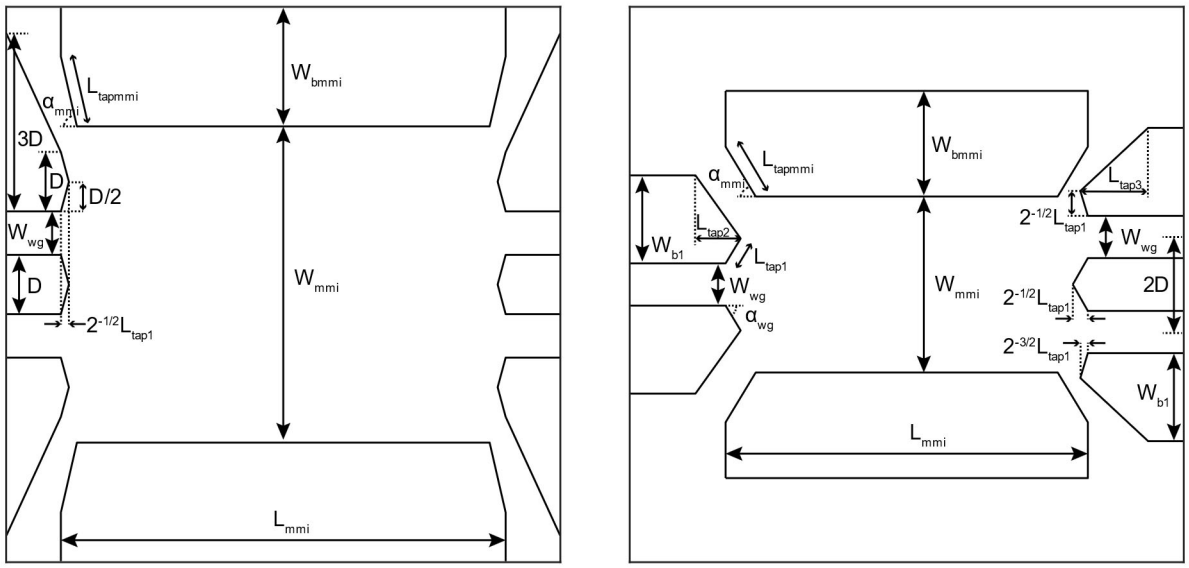

Fig. S2: **Multimode Interferometers.** Detailed design schematics for 2×2 and 1×2 multimode interferometers.

Parameter	**2×2 1050 nm**	**2×2 1550 nm**	**1×2 1550 nm**
L_{mmi} (μm)	23	49	15
W_{mmi} (μm)	7	8	5
W_{bmmi} (μm)	3	3	3
L_{tapmmi}	$2L_{\mathrm{tap1}}$	$2L_{\mathrm{tap1}}$	2
α_{mmi}	45°	45°	45°
D (μm)	0.75	1.5	1.35
W_{wg} (μm)	1	1.1	1.2
α_{wg}	-	-	45°
W_{b1} (μm)	-	-	2.5
L_{tap1} (μm)	1.25	1.25	1
L_{tap2}	-	-	$3L_{\mathrm{tap1}}/\sqrt{2}$
L_{tap3}	-	-	$4.5L_{\mathrm{tap1}}/\sqrt{2}$

Table S1: Geometrical parameters for multimode interferometers.

Note 3: Microcomb pump ring filters

The filter response depends on the intrinsic and coupling Q, as discussed in the main text. Figure S3 shows the variation of coupling Q with the coupling gap between the microring and bus waveguide, calculated using coupled mode theory[6]. The corresponding parameters used are ring radius = 50 μm, ring width = 1.5 μm, and bus waveguide width = 1 μm.

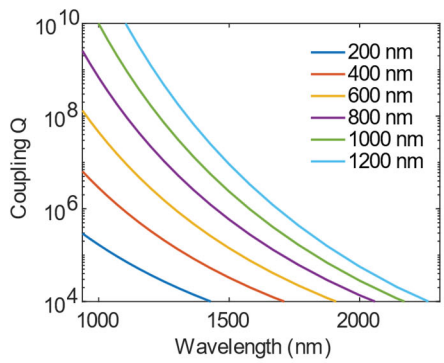

Fig. S3: **Ring filter coupling.** Simulated variation of ring filter coupling Q with coupling gap for a straight bus waveguide. The ring filter is meant to operate around 1550 nm wavelength. For a coupling $Q \approx 10^5$ at 1550 nm, the filter is severely undercoupled at 1000 nm wavelength, as desired, with coupling $Q \approx 5\times10^7$.

Note 4: Dichroic couplers

The dichroic couplers (schematic shown in Fig. S4) used here are based on the strong dispersion, across the octave bandwidth, of the evanescent decay of the optical mode outside the waveguide core. Qualitative starting points for waveguide widths can be found in Fig. S1, which shows the optical confinement and is therefore indicative of the evanescent decay of the fundamental TE modes. Quantitatively, initial device parameters such as waveguide width and coupling gap are determined through finite element-method based eigenmode simulations of the supermodes of uniform couplers. The nominal coupling lengths extracted from these supermode simulations are used as starting points for 3D FDTD simulations that consider S-bends at the input and output of the dichroics. Table S2 shows the design parameters of the two optimized dichroics. Figure S5 shows the variation of dichroic coupler performance, extracted from continuous-wave measurements at wavelengths of 1.05 μm, 1.55 μm, and 2.05 μm. with coupling lengths, with optimal performance measured for the optimized designs.

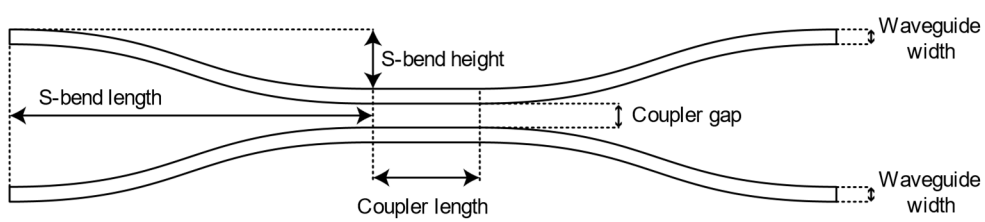

Fig. S4: **Dichroic couplers.** Schematic of dichroic couplers. Dichroic 1 filters out 2 μm light into its cross port, and dichroic 2 filters out 1.55 μm light into its cross port.

Parameter	Dichroic 1	Dichroic 2
Coupler length (μm)	50	170

Coupling gap (μm)	1.25	2.5
Waveguide width (μm)	0.5	0.7
S-bend length (μm)	100	100
S-bend height (μm)	12.5	12.5

Table S2: Geometrical parameters (in μm) for dichroic couplers. Dichroic 1 filters out 2 μm light, and dichroic 2 filters out 1.55 μm light.

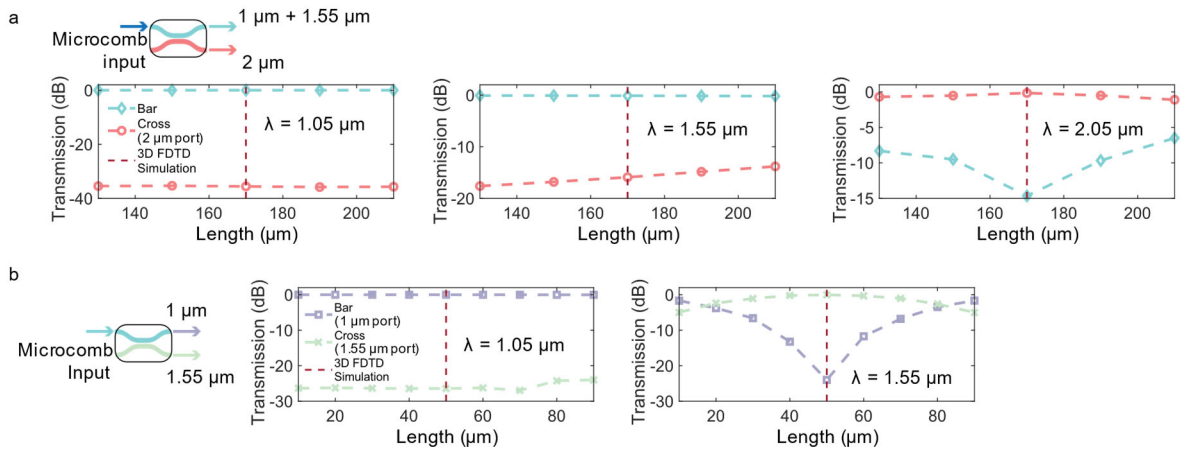

Fig. S5: **Continuous-wave measurements of dichroic couplers. a.** First dichroic, whose purpose is to separate 2 μm light from shorter wavelengths. **b.** Second dichroic, whose purpose is to separate 1.55 μm light from shorter wavelengths. Both dichroics offer optimal performance for coupling lengths that are in agreement with optimized FDTD simulations. The uncertainties in excess loss corresponding to one standard deviation in transmission are less than 0.25 dB at the three wavelengths.

Note 5: Broadband bilayer taper

Figure S6a shows a detailed schematic of the broadband bilayer taper. The transfer of light here requires a balance of the phasematching behind the bilayer coupling across the octave bandwidth. We limit the minimum widths of the tapers in accordance with the corresponding fabrication process (deep-UV lithography), and a broadband 3D FDTD sweep is used to determine the overall taper length. For a taper shorter than the optimal 100 μm, the bilayer coupling is reduced for shorter wavelengths close to 1 μm. Figure S6b shows the tolerance in taper transmission to interlayer thickness and taper misalignment.

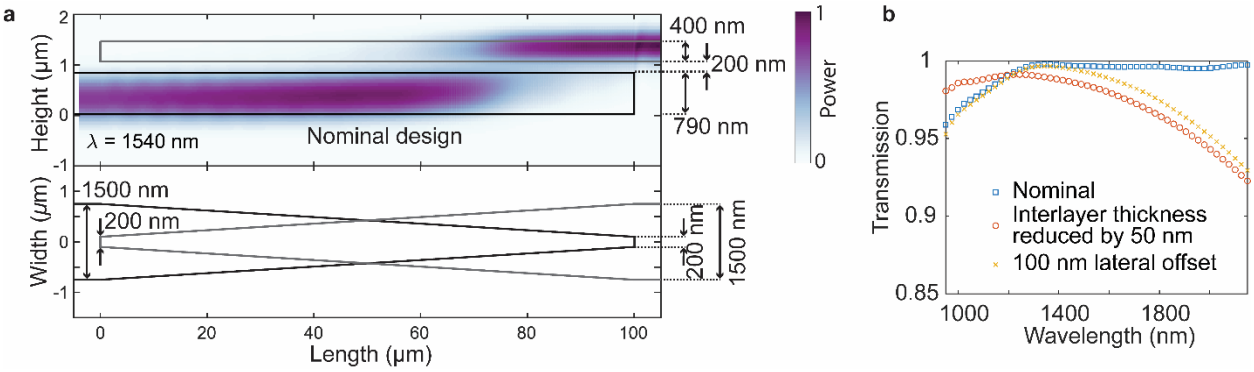

Fig. S6: **Bilayer coupler. a.** Cross section and top views of the bilayer coupler. Both layers are linearly tapered from 200 nm to 1500 nm. **b.** Transmission spectra for a reduced SiO_2 interlayer thickness of 150 nm, and a 100 nm lateral misalignment between the tapers, compared to the nominal design.

A critical step to the successful realization of the bilayer platform in practice is planarization after fabrication of the thick Si_3N_4 layer, after which the interlayer silicon dioxide and interposer Si_3N_4 layers are deposited. Ellipsometry of process control wafers shows a mean interlayer SiO_2 thickness of 204 nm (one standard deviation variation of 4 nm) and a mean top Si_3N_4 thickness of 401 nm (one standard deviation variation of 3 nm). While AFM measurements of the interlayer SiO_2 surface roughness were not performed here, we note that a similar chemical-mechanical polishing process has been recently characterized[7], and an SiO_2 r.m.s. roughness <0.4 nm has been measured.

Note 6: Experimental setups

The experimental setups used are shown in Fig. S7, illustrating the different configurations used for measurements of the multimode interferometers, ring filters, dichroics, integrated spectral microcomb filter, and bilayer microcomb. Each continuous wave laser requires separate fiber components such as the 90:10 splitter and polarization controller, to satisfy the single mode criterion in the fiber. The detector following the 10 % port is used to assist in stabilizing the coupling to the device under test. TE polarization is used throughout all the measurements. Lensed optical fibers with focused spot sizes of ≈ 2.5 μm are used to couple light on and off the chips, aided by inverse tapers on the chips to match the mode profiles between the lensed fibers and waveguides.

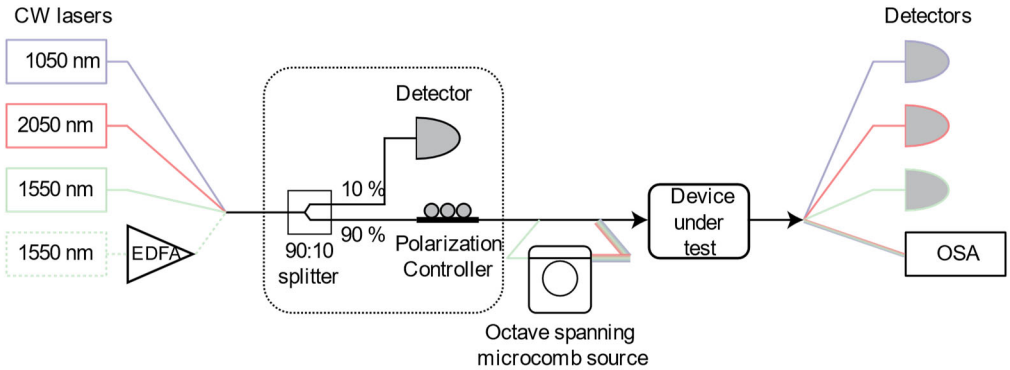

Fig. S7: **Experimental setups.** Multiple experimental setups are used throughout this work, depending on the combination of the device under test and the corresponding inputs. The devices tested are multimode interferometers, ring filters, dichroics, integrated spectral microcomb filter, and the bilayer microcomb. The inputs used are continuous wave lasers at 1050 nm, 1550 nm, and 2050 nm, and an octave spanning microcomb pumped around 1550 nm. Polarization maintaining fiber is used to couple the octave spanning microcomb to the corresponding devices under test. Two OSAs are used to cover the octave bandwidth of the microcomb. EDFA = Erbium-Doped Fiber Amplifier. OSA = Optical Spectrum Analyzer.

The measurement setup used to measure the dichroics with microcomb light consists of a polarization maintaining (PM) connection (2 lensed PM fibers connected by a-meter-long PM fiber using two fiber mating sleeves) between the source microcomb and the dichroics. The PM lensed fibers are rated for a polarization extinction ratio (PER) of 20 dB. The connecting PM fiber is rated for a PER of 25 dB. The two fiber mating connectors are not explicitly rated for PER. The PM fibers we use are 1550 nm XP fibers, rated for operation from 1440 nm to 1625 nm – much less than the octave of bandwidth we use here. We carefully minimize the bending of the fibers to minimize effects of polarization crosstalk and cut-off. Subsequently, our observations of deviations between the experiments and simulations below an extinction level around ≈ –20 dB (Figures 4 and 5 in the main text) are congruent with the PER of the setup. In comparison, the low power continuous wave measurements (Fig. S5) without the use of PM fiber show higher dichroic extinction compared to the microcomb measurements.

Note 7: Summary of expected optical signal distribution in the proposed synthesizer

Figure S8 and Table S3 together show how power would nominally be distributed in the proposed system in the three bands of interest (1 μm, 1.55 μm, and 2 μm). All chip-to-chip coupling losses are conservatively set to 2 dB. For completeness, we show all the elements required for a full system in Fig. S8 – continuous wave pump lasers and microcomb chips (silicon nitride for the THz comb and silica for the GHz comb), alongside the interposer proposed in Fig. 2 of the main text.

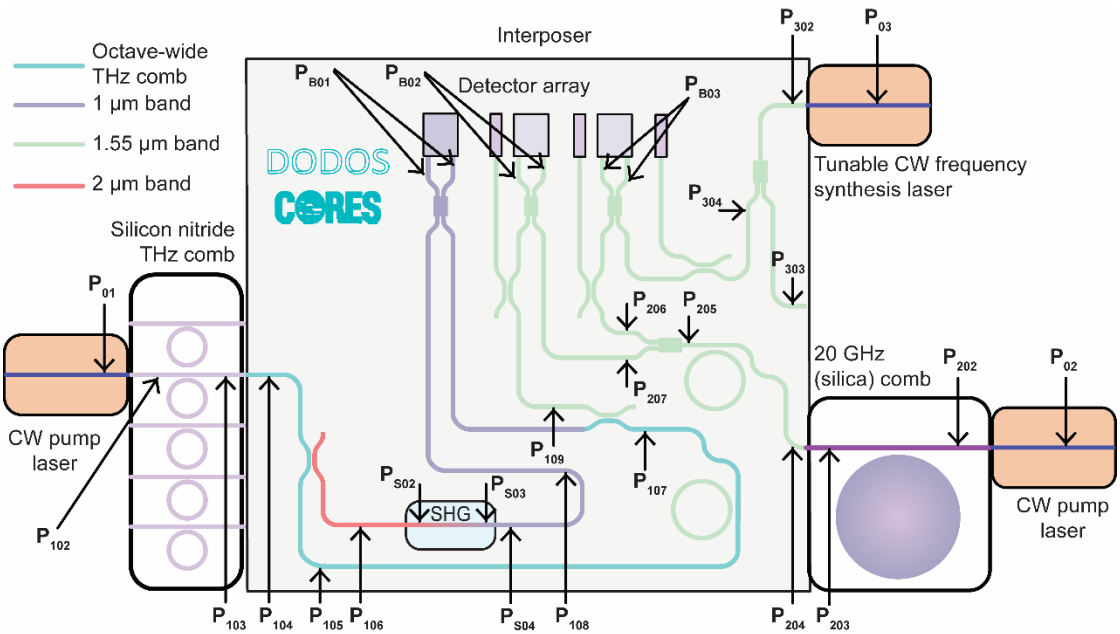

Fig. S8: **Power distribution schematic.** Schematic expanding on Fig. 2 of the main text. The labels showing power distribution throughout the proposed system correspond to Table S3. The schematic indicates how the passive components demonstrated here, i.e., octave-wide dichroics, tunable ring filters, and multimode interferometers, could fit into an interposer and system architecture for a dual-microcomb frequency synthesizer. Chip-to-chip coupled lasers and microcomb sources (silicon nitride and silica) form the dual-microcomb backbone. The THz repetition rate silicon nitride microcomb is used for *f*-2*f* self-referencing via a second harmonic generation-based frequency doubler. Dichroic directional couplers spectrally filter the 1 μm, 1.55 μm, and 2 μm bands of the silicon nitride microcomb. The 20 GHz repetition rate silica microcomb is used for repetition rate stabilization and as a reference for tuning the synthesized output laser. Throughout, multimode interferometers are used to mix signals to generated beat notes for frequency stabilization via balanced detection via fast photodetection. Additional photodetectors are used for power monitoring. In contrast to Fig. 2 of the main text, here the generic 20 GHz frequency comb is replaced by a silica microcomb to best correspond to our envisioned implementation. Alternatively, a 20 GHz silicon nitride microcomb could be considered as well.

Wavelength and power	P_{01} (dBm)	P_{102} (dBm)	P_{103} (dBm)	P_{104} (dBm)	P_{105} (dBm)	P_{106} (dBm)	P_{107} (dBm)	P_{108} (dBm)	P_{109} (dBm)	
1 µm			-20/T	-22/T	-22/T		-22.3/T	-22.3/T		
1.55 µm	22	20	-6/T	-8/T	-8/T		-8/T		-8/T	
2 µm			-8/T	-10/T		-10/T				
Wavelength and power	P_{S02} (dBm)	P_{S03} (dBm)	P_{S04} (dBm)	P_{02} (dBm)	P_{202} (dBm)	P_{203} (dBm)	P_{204} (dBm)	P_{205} (dBm)	P_{206} (dBm)	P_{207} (dBm)
1 µm		-35.3/T	-36/T							
1.55 µm				17	15	-17/T	-19/T	-19/T	-22.2/T	-22.2/T
2 µm	-10.7/T									
Wavelength and power	P_{03} (dBm)	P_{302} (dBm)	P_{303} (dBm)	P_{304} (dBm)	P_{B01} (dBm)	P_{B02} (dBm)	P_{B03} (dBm)			
1 µm					-25.5/T & -39.4/T					
1.55 µm	6.5	4.5	1.3	1.3		-11.2& -25.4/T	-1.9 & -25.4/T			
2 µm										

Table S3: Distribution of optical power throughout the proposed system. /T = per comb tooth

Note 8: Discussion of proposed interposer and synthesizer architecture

In the following note, we provide context for the values shown in Fig. S8 and Table S3. We address power requirements and transmission throughout the proposed system, starting with the lasers themselves, working our way through the microcomb chips, the passive interposer components, the second harmonic generation (SHG) section, the photodetectors, and ultimately end with power considerations for beat note signal-to-noise ratios (SNRs), with an aim to benchmark the performance required of the dichroics, ring filters, and MMIs. We also discuss additional system-level considerations when appropriate.

Note 8.1: Microcomb power levels and compatibility with integrated lasers

We first focus on the spectral power of the octave-spanning microcomb that underpins optical frequency synthesis applications. Figure S9 shows a THz microcomb generated in a Si_3N_4 microring at 100 mW of pump power in the waveguide. The microcomb spectrum is representative of what can be generated after careful optimization of microring dispersion[8,9] and coupling[6] for intrinsic quality factors around 2×10^6. For 2 dB of coupling loss between the microcomb chip and a chip-scale laser, the laser power requirement is around 160 mW, which is achievable from integrated lasers[10]. Dispersive waves at f and $2f$ frequencies help to boost the carrier envelope offset frequency (f_{CEO}) signal.

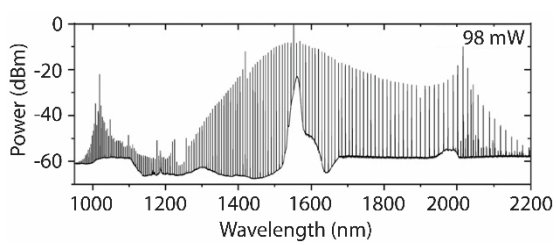

Fig. S9: **Representative THz comb.** This comb is generated using 98 mW of pump power in the Si_3N_4 waveguide.

It has been shown that C-band-spanning comb generation at a 10 GHz to 20 GHz rep rate can be realized with ~30 mW of on-chip pump power, either from silica-based combs[11] or silicon nitride combs[12]. Using a conservative estimate of 2 dB of coupling loss amounts to a power requirement of ~ 50 mW from a chip laser, which is within the performance of chip lasers.

One key consideration common to self-referenced microcomb-based systems is the pinning down of the carrier envelope offset frequency (f_{CEO}) of the microcomb into the bandwidth of the photodetector using for f-2f self-referencing. In the context of the system proposed in Fig. 2 of the main text and Fig. S8 above, this translates to pinning down a THz bandwidth of potential f_{CEO} variation into the nominal 10 GHz bandwidth of the balanced photodetectors. Keeping in mind the ability to prequalify the octave-spanning THz microcomb in schemes like Fig. 2 (where the THz comb chip is separate from the interposer chip), there are a few approaches to managing f_{CEO} appropriately, where f_{CEO} can be measured before system assembly. The first method uses a parametric sweep of the microring radius and width to realize a sweep of f_{CEO}, with approximate tuning rates of 1 GHz/nm and -8 GHz/nm, respectively, for the THz Si_3N_4 microcombs considered here. Sweeping the microring radius is preferred due to its minimal impact on the microring dispersion (and hence the generated comb spectrum). The second relies on thermal tuning, where previously 25 GHz tuning of f_{CEO} has been shown in a 231 GHz repetition rate Si_3N_4 microcomb for a 70°C rise in temperature[13]. Finally, the third is based on post-fabrication trimming of air-clad resonators, which has been previously employed to adjust resonance frequency mismatch and dispersion for four-wave mixing and microcombs[14,15]. From a practical standpoint, it is possible to pattern over 300 microcomb resonators within a 3×5 mm^2 chip, which is sufficient to constrain the 1 THz f_{CEO} variation to the 10 GHz photodetector bandwidth. With sufficient fabrication process control, it should be feasible to eventually monolithically integrate an octave-spanning THz microcomb with appropriate f_{CEO} using a bilayer scheme as shown in Fig. 6 of the main text, particularly if some *in-situ* control (e.g., the thermal tuning) is available.

Note 8.2: First dichroic (2 μm band separation) inhibits two-photon absorption in the gallium arsenide based second harmonic generation waveguide

An integrated synthesizer would require a SHG section that interfaces with a passive interposer. Here, we consider a gallium arsenide (GaAs) based waveguide that can be heterogeneously integrated[16,17] onto the interposer. In this context, one consideration for the first dichroic element that operates on the THz comb is to avoid the potential of strong pump light at 1550 nm causing damage in the expected GaAs SHG element mediated by two-photon absorption (2PA). We use P_{max} to denote the ~ 100 mW pump power. For degenerate 2PA, the 2PA coefficient (β) around 1.55 μm in GaAs is approximately 5 cm/GW[18]. Approximating the modal area by the area of the GaAs waveguide[17] (A_{wg}), 150 nm × 1900 nm, the maximum possible 2PA in the SHG section (ignoring all coupling losses) scales as $(\beta P_{max}/A_{wg})\times(ER_{D1,1.55\mu m})$ which is approximately $0.76\times(ER_{D1,1.55\mu m})$ dB/cm. Here, $ER_{D1,1.55\mu m}$ is the extinction ratio of the 1st dichroic at 1.55 μm. Given that our 1st dichroic has approximately 20 dB of extinction (i.e., $ER_{D1,1.55\mu m} = 0.01$) in the 1.55 μm band, we can rule out any damage and refraction induced by degenerate 2PA. In addition, although non-degenerate 2PA is more complicated to analyze and wavelength-dependent absorption coefficients are not readily available in the literature, the fact that the next-strongest microcomb teeth are weaker in power by 15 dB to 20 dB or more compared to the pump tone implies that non-degenerate 2PA is unlikely to play any significant role.

Note 8.3: Transmission of 2 μm band and SHG power generated in the 1 μm band

Next, we consider the SHG section, comprised of a taper from Si_3N_4 to GaAs, followed by type I SHG in the GaAs waveguide (2 μm TE input and doubled 1 μm TM output), and an asymmetric taper/rotator to transfer light back to the Si_3N_4 and to rotate the doubled 1 μm TM light to TE polarization. The heterogeneous integration of GaAs and Si_3N_4 for our proposed system has been previously reported[16,17]. Within fabrication tolerances, both the input taper and output taper/rotator transmission and rotation efficiency are expected to be >80%, with nominal values of >95% and 90%, respectively[16]. Efficient SHG in a GaAs-on-insulator waveguide (without Si_3N_4 integration) for our proposed system has been reported[17] with a SHG efficiency of 40 W^{-1} (i.e., 4000%/W). Using this nonlinear efficiency, and a conservative estimate of 85% for both Si_3N_4/GaAs transitions, we expect a frequency doubled power of -36 dBm in the 1 μm band.

Note 8.4: Transmission of 1 μm band

The 1 μm band of the THz microcomb traverses the first dichroic, the resonant pump filter, and the second dichroic. The extinction ratio through the first dichroic is approximately > 20 dB, i.e., <1% of the light is rejected. The spectral alignment of the resonant pump filter with the pertinent 1 μm microcomb tooth to be used to measure f_{CEO} is difficult to precisely predict a priori, however, we can calculate the maximum loss possible when the pump filter and comb tooth are perfectly aligned. For a coupling Q of 5×10^7 (see Fig S3), the maximum possible transmission loss is 0.3 dB at 1 μm, calculated using analytic coupled mode theory for an add-drop microring[19] using an intrinsic Q of 1 million. Finally, the second dichroic that extracts 1.55 μm light has an extinction ratio of > 20 dB, i.e., < 1% loss. Cumulatively, we expect > 90% transmission in the worst case of the unwanted alignment between the ring filter and the 1 μm microcomb tooth used for f_{CEO}.

Note 8.5: Transmission of 1.55 μm band

Next, we consider the 1.55 μm band of the THz comb. The first dichroic shows 20 dB of extinction. The extinction offered by the pump filter is tunable and its spurious spectral overlap with the remainder of the THz comb in the *C*-band is alleviated by an intrinsic vernier effect between the THz repetition rate and 478.4 GHz filter FSR. The second dichroic shows 18.5 dB of extinction, implying approximately 97% overall transmission (0.1 dB loss).

Note 8.6: Photodetectors and transimpedance amplifiers:

Finally, we need to consider the performance of the photodetectors and transimpedance amplifiers (TIAs) to quantify the role of the performance of the passive interposer components at a system level. Photodetectors heterogeneously integrated on Si_3N_4 (without TIAs) suited for our system have been reported[20] with responsivities of 0.83 A/W and 0.94 A/W in the 1 μm and 1.55 μm bands, respectively. Balanced photodetectors show common mode rejection ratios > 40 dB and bandwidths of 10 GHz. Single photodetectors show bandwidths of 20 GHz and dark currents of 20 nA, sufficient to directly detect the repetition rate of the 20 GHz silica microcomb with SNR well in excess of 30 dB. In addition, photodetectors integrated on a printed circuit board with TIAs (no heterogeneous integration with Si_3N_4) have been reported[21] where two designs show bandwidths around 10 GHz, maximum conversion gains between 1289 to 2083 V/W, and minimum noise equivalent powers (NEPs) of 13 $pW/\sqrt{Hz}$. Details regarding recent progress in the TIAs can be found in Ref. 22. Furthermore, a heterodyne receiver-based approach to tackle potential SNR limitations in optical comb power was previously reported in Ref. 23.

Note 8.7: Pump laser extinction ratios

The main consideration in determining the extinction applied to the pump lasers by the tunable ring filters is the need to not saturate, or worse, damage, the photodetectors. At the same time, there is a question of how much extinction is sufficient and can let the rest of the system operate unimpeded. Our approach has been to filter the pump to match the adjacent comb teeth – for the THz comb, this power level is intrinsically compatible with the subsequent dichroic filtering (at the 2nd dichroic) prior to beat note detection. For the 20 GHz comb, this level of pump filtering also avoids an excessive dynamic range requirement when measuring the beat note between the 20 GHz comb and the tunable synthesis laser. On the other hand, if, for example, the 20 GHz comb pump was entirely filtered out (with say 100 dB of extinction), there would be a discontinuity between comb teeth around the pump, and consequently also in the tuning range of the synthesis laser that is referenced to the 20 GHz comb.

Note 8.8: Beat note SNRs

There are three beat notes to be detected for stabilization and synthesis – the carrier envelope offset frequency f_{CEO}, the inter-comb beat note for locking the two combs (hereafter referred to as dual comb lock (DCL) for brevity), and the offset between the tunable laser and the silica comb (hereafter referred to as tunable laser lock (TLL) for brevity) for synthesis. The 20 GHz repetition rate of the silica microcomb is directly detected, as

discussed in Note 8.6. In the following estimates of the SNRs of these three beat notes, we use a conservative NEP of 20 pW/$\sqrt{\text{Hz}}$ (see Refs. 20 and 21) and optical powers and system parameters as shown in Fig S8 and Table S3. First, we consider the variation of the CEO SNR with the detection bandwidth, shown in Fig. S10, which illustrates a tradeoff – between the high SNR offered by low detection bandwidths and the low SNR caused by the need for higher bandwidths required to operate a standalone system. Using a broadband radiofrequency (RF) mixer and a swept intermediate frequency (IF) for RF down-conversion followed by a narrow low pass filter (LPF) can offer an intermediate resolution to this tradeoff, with a nominal 5 MHz of bandwidth (from the low pass filter) and corresponding 16.9 dB of CEO SNR. If we relax the conservative coupling loss estimates to 1 dB from 2 dB, we expect the CEO SNR to increase to 25.5 dB, based on increases in microcomb power and increased SHG. The DCL SNR and TLL SNR are estimated to be 25 dB and 31.1 dB, respectively, when both detected using 50 MHz bandwidth using a similar swept IF RF downconversion with a LPF[23].

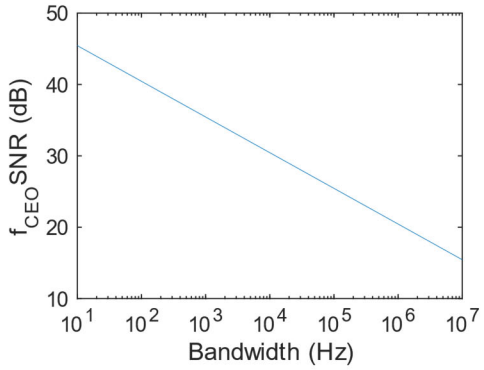

Fig. S10: **Calculated signal-to-noise ratio of carrier envelope offset frequency in proposed synthesizer**. Variation with detection bandwidth.

Note 8.9: Impact of dichroic and MMI performance on beat note SNRs:

Figure S11 shows the impact of the dichroics' performance on the CEO and DCL SNR. The TLL SNR is unaffected by the dichroics. For the CEO SNR calculation, we assume that the extinction ratios for the 1 μm band are the same at the 1st and 2nd dichroic, for ease of representation. 3 dB of extinction would imply 50:50 splitting.

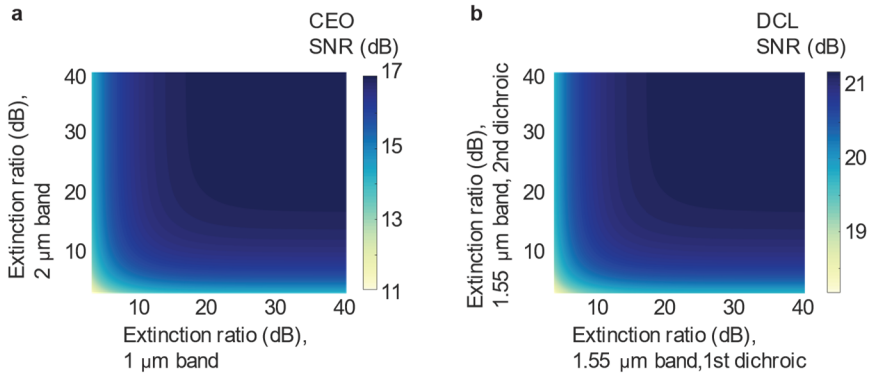

Fig. S11: **Calculated signal-to-noise ratio of carrier envelope offset frequency and dual comb locking in proposed synthesizer**. Variation with dichroic performance.

While significantly worse dichroic extinction would decrease the CEO and DCL SNRs to different extents, an increase in the dichroic extinction ratios even up to 40 dB from the current ~ 20 dB will have comparatively negligible improvement in the SNRs. Thus, the current performance of the passive interposer components would not be the limiting factor in increasing the CEO and DCL SNRs. Other factors, such as increasing the THz

pump power to its maximum of 250 mW[10], increasing the SHG efficiency, and decreasing the NEP of the photodetectors, would have to drive increases in SNR. Overall, this is reasonable when considering the excellent progress in integrated photonics, for example, SHG efficiencies have steadily increased across different material systems. Outside of the photonic devices, reducing the electronic bandwidth after detection will improve SNR, as discussed in Note 8.8.

The MMIs have two functions in the proposed interposer system - the first is to split power (1x2 MMIs), and the second is coherent mixing (2x2 MMIs). While only the 1 μm band 2x2 MMI is used for the CEO beat note, the beat notes for dual comb locking and tunable laser locking involve 2 and 3 MMIs in the 1.55 μm band. The impact of MMI excess loss (Fig. 3b, main text) on the beat note SNRs is shown in Fig. S12.

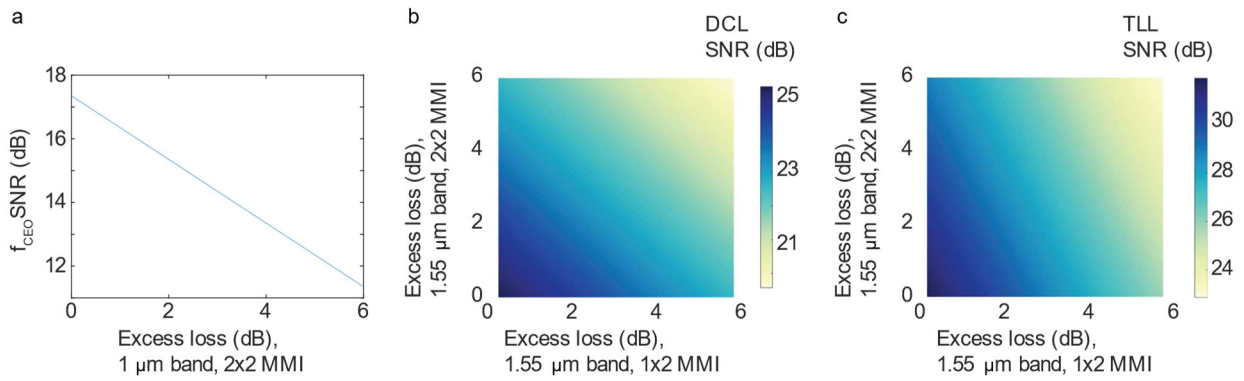

Fig. S12: **Calculated signal-to-noise ratio of carrier envelope offset frequency, dual comb locking, and tunable laser locking for the proposed synthesizer**. Variation with MMI performance.

Similar to the dichroics, any improvement in the demonstrated excess loss of the MMIs would lead to only a small increase in beat note SNRs, while an increase in overall system optical power and transmission, and a decrease in photodetector noise would improve the beat note SNRs significantly.

References

1. M.-C. Tien et al, "Ultra-low loss Si_3N_4 waveguides with low nonlinearity and high power handling capability," Opt. Express **18**, 23562-23568 (2010).
2. K. Y. Yang et al, "Bridging ultrahigh-Q devices and photonic circuits," Nat. Photon. **12**, 297–302 (2018).
3. M. A. Tran, D. Huang, and J. E. Bowers, "Tutorial on narrow linewidth tunable semiconductor lasers using Si/III-V heterogeneous integration," APL Photonics 4, 111101 (2019).
4. L. B. Soldano and E.C. Pennings, "Optical Multi-Mode Interference Devices Based on Self-Imaging: Principles and Applications," Journal of Lightwave Technology **13**, 615–627, (1995).
5. E. Kleijn et al, "Multimode interference couplers with reduced parasitic reflections," IEEE Photonics Technology Letters **26**, 408–410 (2014).
6. G. Moille et al, "Broadband resonator-waveguide coupling for efficient extraction of octave-spanning microcombs," Optics Letters **44**, 4737–4740 (2019).
7. L. Chang et al, "Heterogeneous integration of lithium niobate and silicon nitride waveguides for wafer-scale photonic integrated circuits on silicon," Opt. Lett. **42**, 803–806 (2017).
8. Q. Li et al, "Stably accessing octave-spanning microresonator frequency combs in the soliton regime," Optica **4**, 193-203 (2017).
9. T. C. Briles et al, "Interlocking Kerr-microresonator frequency combs for microwave to optical synthesis," Opt. Lett. **43**, 2933–2936 (2018).
10. https://freedomphotonics.com/freedom-photonics-products/lasers-and-laser-sources/1550-nm-high-power-dfb-laser-fp3815/
11. X. Yi, Q.-F. Yang, K. Y. Yang, M.-G. Suh, and K. Vahala, "Soliton frequency comb at microwave rates in a high-Q silica microresonator," Optica **2**, 1078-1085 (2015).
12. J. Liu et al, "Photonic microwave generation in the x-and k-band using integrated soliton microcombs," Nat. Photonics **4428**, 1–6 (2020).
13. X. Xue et al, "Thermal tuning of Kerr frequency combs in silicon nitride microring resonators," Opt. Express **24**, 687-698 (2016).
14. X. Lu et al, "Efficient telecom-to-visible spectral translation through ultralow power nonlinear nanophotonics," Nat. Photonics **13**, 593–601 (2019).
15. G. Moille et al, "Post-Processing Dispersion Engineering of Frequency Combs in Microresonator Addressing Atomic Clock," in *Conference on Lasers and Electro-Optics*, OSA Technical Digest (Optical Society of America, 2020), paper SW3J.5.
16. E. J. Stanton et al, "On-chip polarization rotator for type I second harmonic generation," APL Photonics **4**, 126105 (2019).
17. E. J. Stanton et al, "Efficient second harmonic generation in nanophotonic GaAs-on-insulator waveguides," Optics Express **28**, 9521-9532 (2020).
18. W. C. Hurlbut et al, "Multiphoton absorption and nonlinear refraction of GaAs in the mid-infrared," Optics Letters **32**, 668-670 (2007).
19. C. Manolatou et al, "Coupling of modes analysis of resonant channel add-drop filters," IEEE Journal of Quantum Electronics **35**, 1322–1331 (1999)
20. Q. Yu et al, "Heterogeneous photodiodes on silicon nitride waveguides," Opt. Express **28**, 14824-14830 (2020).
21. R. Costanzo, Z. Yang, A. Beling, and S. M. Bowers, "Wideband Balanced Photoreceivers With InP-Based Photodiodes and 65 nm CMOS TIAs for Use in Optical Frequency Synthesis Systems," Journal of Lightwave Technology **37**, 5833 - 5839 (2019).
22. R. Costanzo and S. M. Bowers, "A 10-GHz Bandwidth Transimpedance Amplifier With Input DC Photocurrent Compensation Loop," IEEE Microwave and Wireless Components Letters **30**, 673-676 (2020).
23. A. Bluestone et al, "Heterodyne-based hybrid controller for wide dynamic range optoelectronic frequency synthesis," Opt. Express **25**, 29086-29097 (2017).